MEASUREMENTS OF ELECTRON ENERGY DISTRIBUTION FUNCTION AND NEUTRAL GAS TEMPERATURE IN AN INDUCTIVELY COUPLED PLASMA

A Thesis Submitted to the College of

Graduate Studies and Research

In Partial Fulfillment of the Requirements

For the Degree of Master of Science

In the Department of

Physics and Engineering Physics

University of Saskatchewan

Saskatoon

By

HONG LI

Keywords: plasma, ICP, electron energy distribution function, neutral gas temperature

PERMISSION TO USE

In presenting this thesis in partial fulfilment of the requirements for a Postgraduate degree from the University of Saskatchewan, I agree that the Libraries of this University may make it freely available for inspection. I further agree that permission for copying of this thesis in any manner, in whole or in part, for scholarly purposes may be granted by the professor or professors who supervised my thesis work or, in their absence, by the Head of the Department or the Dean of the College in which my thesis work was done. It is understood that any copying or publication or use of this thesis or parts thereof for financial gain shall not be allowed without my written permission. It is also understood that due recognition shall be given to me and to the University of Saskatchewan in any scholarly use which may be made of any material in my thesis.

Requests for permission to copy or to make other use of material in this thesis in whole or part should be addressed to:

Head of the Department of Physics and Engineering Physics

University of Saskatchewan

Saskatoon, Saskatchewan S7N5E2

ABSTRACT

Inductively coupled plasma (ICP) is a promising low pressure, high density plasma source for material processing and is of great importance to modern plasma technology. This thesis summarizes the results of experimental study in a cylindrical ICP by using a single Langmuir probe (LP) and optical emission spectroscopy (OES).

The electron energy distribution function (EEDF), which contains important information of ICP plasma and is necessary for an accurate kinetic description of the low-pressure discharges, has been investigated with the Langmuir probe by using the alternating current (ac) method. Measurements were carried out in different gases including both atomic (argon, helium) and molecular (hydrogen, nitrogen) gases. The effects of the external discharge parameters such as gas pressure and radio frequency (rf) power have been investigated and the different mechanisms that influence the formation of the EEDF have been discussed. The radial dependence of the EEPF in the argon plasma has also been evaluated.

The average electron energy and electron density have also been obtained by direct measurement of the electron current-voltage (I-V) curve and the result is consistent with the power balance equation.

Optical emission spectroscopy has been used to study the importance of neutral gas heating in the ICP. The method used is based upon simulating and fitting the nitrogen emission band (the transition from $C^3\Pi_u, V'=0$ to $B^3\Pi_g, V''=0$). Both nitrogen and argon plasmas have been studied separately and significant neutral heating has been found.

ACKNOWLEDGMENTS

TABLE OF CONTENTS

LIST OF TABLES

LIST OF FIGURES

LIST OF SYMBOLS

a_{1m} The m_{th} zero of the first order Bessel function

A_{eff} Effective area for particle loss

B Susceptance

$\dot{B}$ Magnetic flux density

C Capacitance

d_{eff} Effective plasma size

D_ε Electron energy diffusion coefficient

e Electron charge

E Total energy of the molecule

E_{diss} Dissociation energy of molecule

E_e Electric energy

E_i Ionization energy

E_{is} Ionization energy of molecule

E_{mn} Fourier-Bessel component of the inductive field

E_R Rotational energy

E_V Vibrational energy

$f(\mathbf{v})$ Electron velocity distribution function

$f(\varepsilon)$ Electron energy probability function

$f_D(\varepsilon)$ Druyvesteyn electron energy distribution function

$f_E(\varepsilon)$ Electron energy distribution function

$f_M(\varepsilon)$	Maxwellian electron energy distribution function
$I(J', J'')$	The spectrum intensity
J	Rotational quantum number
k	Boltzmann's constant
k_{12}	Collision rate
k_e, k_v, k_R	Wave number of electronic, vibrational, and rotational state respectively
K_{iz}	Ionization reaction rate
L	Plasma source length
m	Mass of the electron
M	Mass of the ion
n_e	Electron density
n_i	Ion density
N_g	Neutral number density
P	Gas pressure
P_{abs}	Power absorbed by the plasma
R	Plasma source radius
S	Probe surface area
$S(J', J'')$	Line strength factor
T_e	Electron temperature
T_{eff}	Effective electron temperature
T_g	Neutral gas temperature

T_i	Ion temperature
T_{rot}	Rotational temperature
v_{12}	Relative velocity of particle 1 with respect to particle 2
v_e	Electron average flow velocity
v_i	Ion average flow velocity
V	Electric potential
V' , V''	Vibrational quantum number of molecule
V_f	Floating potential
V_p	Plasma potential
W	Full width at half maximum
X	Reactance
ε	Electron energy
$\langle \varepsilon \rangle$	Average electron energy
ε_L	Total energy loss per ion lost from the system
ε_c	Energy loss per ion-electron pair
ε_i	Energy transferred from the plasma to the chamber by ions
ε_e	Energy transferred from the plasma to the chamber by electron
$\Theta(\dfrac{q_n v}{\omega}, \dfrac{v}{\omega})$	The interaction between an electron with thermal velocity v and the electric filed E_{mn}
λ_{12}	The mean free path of particle 1 in a medium of particle 2

λ_D	Debye Length
λ_{en}	Electron-neutral mean free path
ρ	Charge density
σ_{12}	Collision cross-section between species 1 and 2
σ_{en}	Momentum transfer cross section for electron-neutral collisions
χ^2	Chi-square
ω	Oscillation frequency
ϖ_e	Vibrational frequency

Chapter 1

Introduction

1.1 Roles of Plasmas in Materials Processing

Plasma is an ionized gas composed of charged ions, either positive or negative, electrons, and neutral particles that grossly maintains charge neutrality [1]. Ionization of neutral atoms and molecules requires bombardment of energetic electrons on them and a plasma can be maintained only at a high temperature, typically higher than 1 eV. Ions, electrons and neutrals in a plasma can have different temperatures depending on the collision frequencies among them. Plasmas used for material processing exploit this temperature disparity. For example, in the case of plasma reactors used for etching, low temperature ions are accelerated through a sheath in which the potential drop is governed by a high electron temperature. Plasmas used in material processing are not in thermal equilibrium and energy distribution of each species may not necessarily be Maxwellian.

Plasma-based surface processing is indispensable for high-technology industries including large scale integrated circuits, surface coating, ion implantation, solar cells, etc. [2]. The Moore's law (see Fig.1.1) in microelectronics industry is still holding largely due to the advancement in microlithography and plasma based manufacturing technologies. The ruler scale is now approaching 30 nanometers at which the conventional chemical etching becomes totally useless.
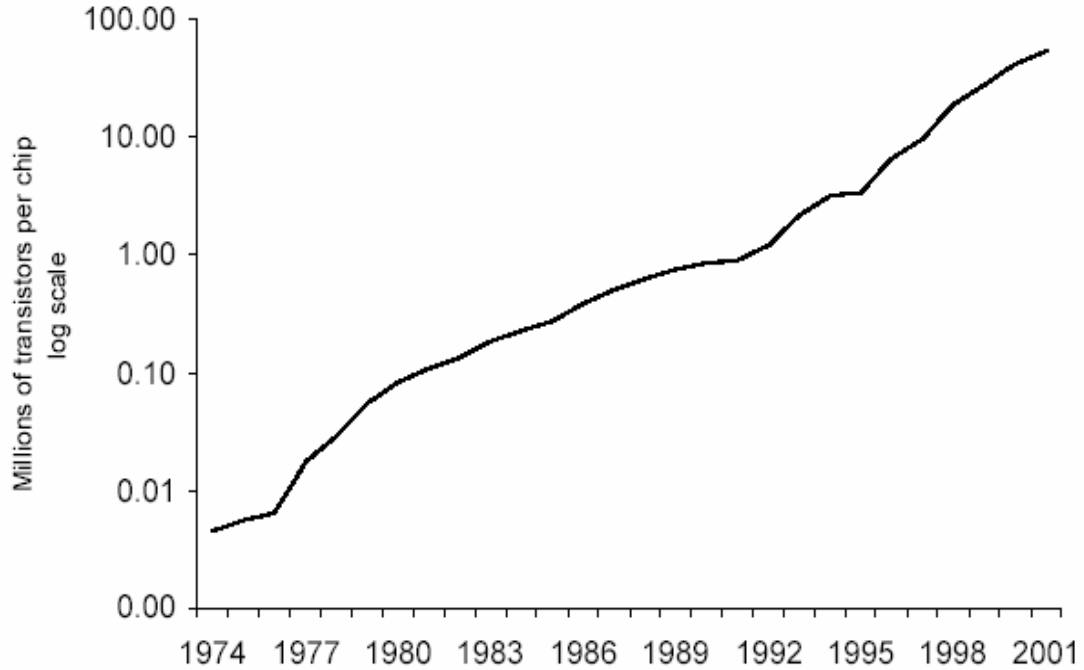
Figure 1.1   Illustration of Moore's Law (number density of transistors doubling every two years. From: http://en.wikipedia.org/wiki/Moore's_law).

Plasmas used in materials processing are weakly ionized gases rich with chemically active radicals. They provide active environment for plasma chemistry characterized by high plasma density and high electron temperature that are not available in the conventional chemical processing methods. As mentioned briefly above, the high electron temperature in processing plasmas is in fact responsible for active plasma chemistry because ions gain energy through acceleration in the sheath, which maintains a potential drop characterized by the electron temperature [3]. An electron temperature higher than the ion (and neutral) temperature in processing plasmas is possible because electrons are heated by an electric field externally applied and temperature equilibration with ions does not occur because of insufficient collisions and the low efficiency in transferring kinetic energy to ions during collisions. The energetic electrons thus

2

produced by an electromagnetic field will further induce ionization and dissociation reactions, which will generate reactive species in the plasma. Thus, it is possible that in processing plasmas, chemical reactions, which normally would require high electron temperatures, can occur in an environment with relatively low ion and neutral temperatures. Furthermore, due to their much higher thermal velocities than those of the ions, the fast-moving electrons will rapidly be lost to the walls of the plasma and the plasma potential becomes elevated from the wall potential. A thin layer, called plasma sheath, will be formed near the wall in which the ion densities are much greater than the electron densities, that is $n_i \gg n_e$. The net positive charge within the sheath leads to a potential that is positive in the plasma and drops sharply to zero near the grounded wall. Positive ions are accelerated in the sheath while electron loss rate is reduced to match the ion loss rate due the same sheath potential relative to the plasma. This leads to directional bombardment of the surface by energetic ions.

1.2 Basic Properties of Plasma

At a sufficiently high temperature, all atoms and molecules are fully ionized. However, such fully ionized plasmas are not very useful for plasma processing because of the absence of radicals, which promote plasma chemistry. Partially ionized plasmas are characterized by an electron temperature in the range of 1 to 10 eV and can be produced by various means, including dc electrode discharge, capacitive discharge, electrode-less inductive coupling, microwave, arc discharge, etc.. Generally, the plasmas used in materials processing are in non-local thermal equilibrium (non-LTE) state. The electron temperature in non-LTE plasmas is higher than that of ions (and neutrals) because of insufficient collisions. In addition, the energy distribution functions of electrons and ions

are not necessarily Maxwellian also because of insufficient collisions among like particles (e.g., electron-electron collisions). Charge neutrality is maintained except in the ion rich sheath which necessarily develops in the plasma to satisfy ambipolarity (equal current of ions and electrons to the wall to maintain charge neutrality) near the vacuum chamber wall.

1.3 Motivation for, and Objectives of the Project

The study of plasma-material interactions has evolved into an important and dynamic field of research. Processing plasma is a complex system and many issues still remain unresolved. There are two aspects of plasmas which are important in plasma processing: physical and chemical. The physical effects resulting from the plasmas are caused by the arrival at the sample of electrons and ions [4]. They may affect the substrates significantly if the charged particles have sufficient energy. The chemical effects of plasmas result from the chemical activity of species such as ions and radicals that are generated in the plasma by electron collision with molecules. So development of plasma technologies depends on a better understanding of the physical and chemical plasma processes [2, 5, 6], which are directly related to the electron energy distribution function (EEDF). EEDF is a measure of the number of electrons within a unit energy interval. EEDF in processing plasmas often deviates markedly from Maxwellian distribution and knowing EEDF in a given plasma is necessary to calculate various cross-sections for physical and chemical reactions [7, 8].

In most of the low-pressure discharges used for materials processing, electrons absorb energy of externally applied electromagnetic field. Ionization, dissociation and excitation of molecules are rendered by collisions with energetic electrons. The electrons

4

also transfer kinetic energy to ions through collisions. In the low pressure discharges, although the densities of ions and electrons may be much lower than that of the neutrals, the charged particles play central roles in sustaining the discharge and producing radicals needed for chemical reactions. Since $T_e >> T_i$, it is the electrons that dissociate the feedstock gas to create the free radicals, etchant atoms, and deposition precursors that are required for the chemistry at the substrate. Electrons also ionize the gas to create the positive ions that subsequently bombard the substrate. The average electron temperature T_e is usually smaller than the threshold energies E_{diss} or E_{is} for dissociation and ionization of the feedstock gas molecules. Nevertheless, dissociation and ionization can occur because there is a significant number of high energy electrons in the tail region of electron energy distribution [2].

To fully characterized a plasma, it is important to know the energy distribution of the electrons, which is not only directly connected to the chemistry of the electronic kinetic processes within bulk plasma but also implicitly connected with the internal plasma parameters like electron density, temperature and so on [9, 10]. Knowing the electron energy distribution function is also the only way to get a better understanding of the kinetic processes within the bulk plasma especially when more reliable data for inelastic cross section for various chemical reactions are absent [8]. Knowledge of the electron energy distribution function will also provide valuable information of power absorption [11, 12] and the rate of ionization by electron collisions and so on [13].

Recently, there have been many studies [9-10, 14-24] on measurement of the plasma characteristics in inductively coupled plasmas (ICPs). However, due to the device specifics of the ICP characteristics, it is still difficult to determine the relationship

between the external parameters (like gas flow rate, gas pressure and radio (rf) power, etc.) and the internal ones (like average electron energy, plasma density, etc.) of ICPs. All those internal parameters are important in designing a practical ICP device and to control the device performance. In materials processing, the desired results such as uniformity of etch and deposition rate depend on the internal parameters of plasmas, which on the other hand, depend on the discharge geometry and externally adjustable parameters like rf power, process gas and gas pressure. Thus, it is important to know the interdependence of the internal and external parameters. Currently, there are different opinions about the structure of the EEDF in ICPs. EEDF in ICP tends to be either Maxwellian distribution or Druyvesteyn distribution. Furthermore, most of the work has been focused on the inert gas argon and only little work was done for the molecular gases such as nitrogen and hydrogen, which are promising gases for plasma processing.

Regarding the kinetics of neutral particles in a processing plasma, it has been recently found that, in ICPs, heating of neutral species is significant and gas temperatures may exceed by a large margin the room temperature [25-36]. Knowing the neutral temperature is also important, for it is one of the key factors that control the electron number density and temperature. According to the work in Ref [37], the increase of the neutral gas temperature has an almost similar effect on the plasma parameters as the decrease of the gas density, which tends to lead to a higher electron temperature but a lower number density. Notable distortions of the neutral number densities will occur due to heating of the neutral species in ICP; this non-uniformity will further change other plasma parameters such as temperatures and number densities of the reactive species, and the chemical reactions [38].

1.4 Experimental Methodology and Main Results

Electron energy distribution function has been measured using a single Langmuir probe (LP). Measurements have been carried out over a wide range of gas pressures, discharge powers, and spatial positions. The ac (alternating current) method [39, 40] is used to obtain EEDF in various plasmas with different gases. In argon discharges, EEDF shows a two-temperature Maxwellian structure at low pressures (in the regime of 1 mTorr) and becomes Druyvesteyn-like at higher pressures above 10 mTorr. For discharges in molecular gases (diatomic) like hydrogen and nitrogen, EEDF deviates markedly from both the Maxweillian and Druyvesteyn distribution, especially at a relatively high pressure and low discharge power. Some other plasma parameters, including electron temperature and density have also been found.

Dependence of the neutral gas temperature on the gas pressure and discharge power in inductively coupled plasma source has been investigated by using optical emission spectroscopy (OES) [25, 26]. The neutral gas temperature has been determined by simulating and fitting the rotational nitrogen emission band (the transition from $C^3\Pi_u, V'=0$ to $B^3\Pi_g, V''=0$). Both nitrogen and argon plasmas have been studied. In the case of argon plasma, about 5% nitrogen was added to the argon gas flow as an actinometer. The maximum temperature of Ar gas was found to be as high as 1850 K at 1 Torr working pressure and 600 W rf power. The temperature increases almost linearly with the logarithm of the gas pressure, but changes only slightly with the discharge power in the range of 100-600 W.

In the nitrogen plasma, a sudden decrease in the neutral gas temperature occurs when the gas pressure is increased and the discharge power is fixed. This corresponds to

a discharge mode transition from H-mode (high plasma density) to E-mode (low plasma density). The discharge mode transition can also be verified by the transition of the plasma density measured by Langmuir probe. In the H-mode, the gas temperature is proportional to the logarithm of the gas pressure as in argon plasma. The gas pressure at which the transition occurs increases with the discharge power. In contrast to the case of argon plasma, the gas temperature in the nitrogen discharge increases almost linearly with the discharge power. The electron density in nitrogen plasma is about 10% of that in argon plasma. This may explain the observation that the nitrogen neutral temperature is always lower than the argon neutral temperature under the same discharge power and gas pressure.

1.5 Thesis Outline

This thesis deals with two main subjects. One is the characterization of a low-pressure inductively coupled plasma by using Langmuir Probe (LP). The other is to measure the neutral gas temperature with the Optical Emission Spectroscopy (OES) in both argon discharge and nitrogen discharges.

Chapter 2 describes the ICP plasma source used in this study. Chapter 3 presents details of the Langmuir probe theory in low temperature plasma diagnostics. The method used to reveal EEDF is also explained. In Chapter 4, the results of LP measurements are presented, including the electron density, electron temperature, electron energy distribution function and plasma potential. Chapter 5, constituting the second part of this thesis, deals with the neutral gas temperature measurement by measure of optical emission spectroscopy (OES). A brief description of the molecular theory is given followed by the experimental results. Significant neutral heating observed and plausible

mechanisms are discussed. In chapter 6, the findings made in the project are summarized. Suggestions for future work conclude the thesis.

Chapter 2

Inductively Coupled Plasma

2.1 Introduction

Plasma production by inductive coupling of rf waves has been known over a century. Hittorf, in 1884, was the first to report on inductive discharge, which was described as an "electrode-less ring discharge" [2, 41]. In 1942, G.I. Babat [41] for the first time succeeded in sustaining electrode-less ICPs at atmospheric pressure and drew a clear distinction between capacitive discharges excited by the electric field (E-discharges) and eddy discharges excited by the alternating magnetic field (H-discharges). About 20 years later, Reed [42] described ways of maintaining argon ICPs in 'open vessels' (torches). Eckert [3] reviewed the developments that focused on gas pressure exceeding 20 mTorr in cylindrical coil geometry. In the late 1980s, the planar coil configuration was developed [41].

Inductively coupled discharges are now the leading plasma sources for plasma processing because of the simplicity of concept and no requirement of constant magnetic field, which is necessary in electron cyclotron resonance (ECR) and helicon discharges. Additional advantage is that a relatively high density plasma can be produced and the ion energy can be controlled by adding an extra biasing to substrate holders without affecting plasma production.

2.2 Basic Principle of Inductively Coupled Plasma and Typical Configurations

Inductively coupled plasma (ICP) sources have been developed in order to overcome the drawback of capacitively coupled plasma (CCP), namely, the difficulty in independently controlling particle density and energy due to the design of CCP. As shown in Fig. 2.1, the CCP usually consists of two metal electrodes, separated by a small distance, placed in a reactor. One of these two electrodes is connected to a power supply, and the other one is grounded. The self bias voltage that is always created on the driven electrode in a capacitively coupled rf discharge leads to the difficulty in independently controlling the ion energies [43].
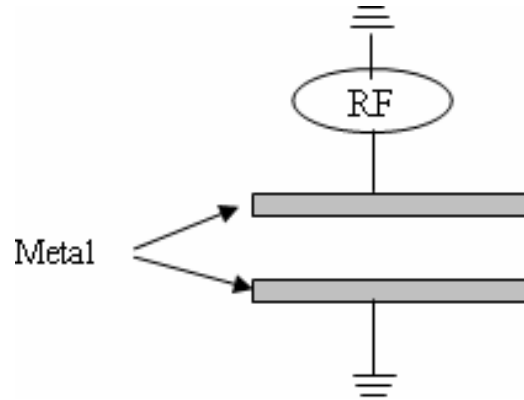
Figure 2.1   Capacitively Coupled Plasma source.

Figure 2.2(a) shows a typical diagram of an ICP. In order to generate an ICP, an rf current is passed through an antenna and the fields penetrate a dielectric wall into the region where a plasma is formed. According to Faraday's law, the time-varying axial magnetic flux density, $\dot{B}$, induces an azimuthal electric field as shown in Fig. 2.2(b).
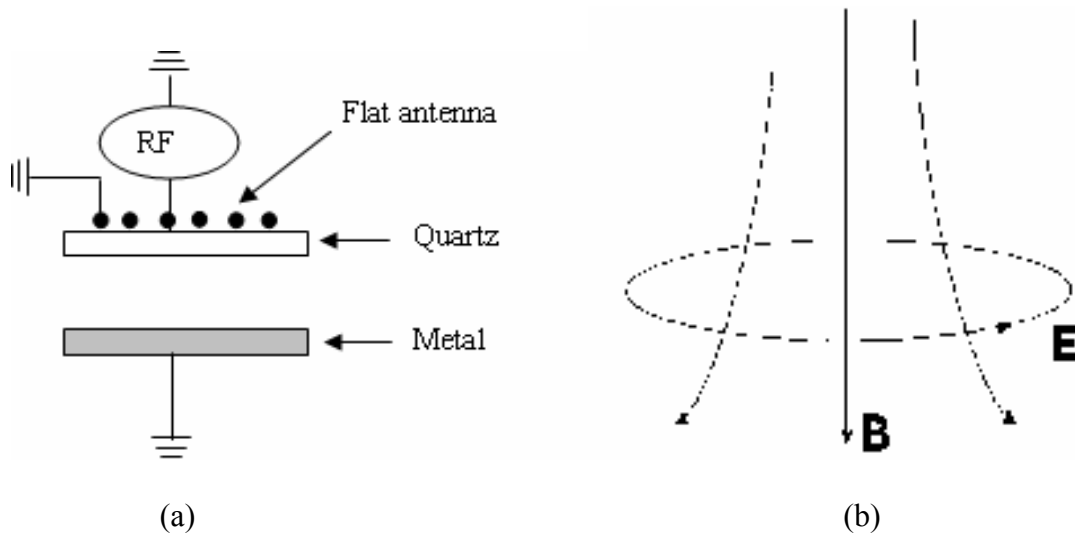
Figure 2.2   (a) Inductively coupled plasma and (b) the corresponding electric and magnetic field.

The electric field accelerates electrons which absorb energy. They are thermalized and acquire an average energy of 1 to 10 eV in ICP. Through collisions, electrons further ionize the gas. Because of the large mass compared with that of electrons, ions do not gain energy directly from rf field. However, ions are accelerated in the sheath potential and ions falling on the vacuum chamber wall may have a kinetic energy corresponding to the plasma potential. The ion energy can be controlled by adding an extra biasing. Typical gas pressures in ICP devices are below 50 mTorr, while the electron densities are relatively high (10^{10} -10^{12} cm^{-3}). Furthermore, as in CCP sources, the electron temperature is much higher than that of the ions in ICPs, namely, ICPs are non-LTE plasmas. An ICP usually has one conducting plate to hold substrates. Such a plate is needed to provide a potential reference to the plasma.
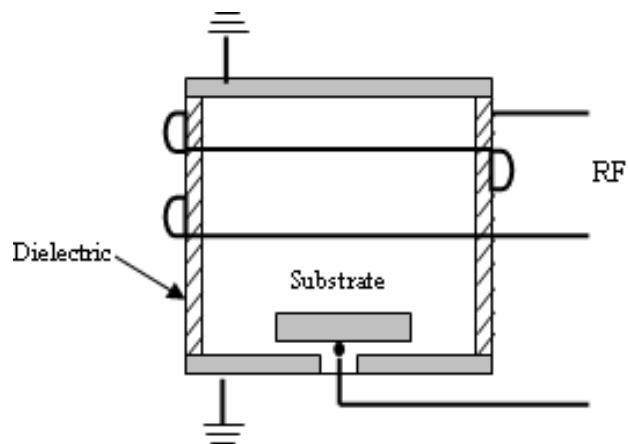
Figure 2.3   Schematic diagram of inductively driven source: cylindrical geometry.

Two common ICP coil configurations, planar and cylindrical, are shown in Figure 2.2 and 2.3 respectively. The planar coil is a flat spiral wound from near the axis to the outer radius of the discharge chamber. Inductive coils are commonly driven at 13.56 MHz or lower, usually using a rf supply through an impedance matching network.

2.3 ICP Reactor in the Plasma Physics Laboratory

The ICP system used in the experiment is shown in Fig. 2.4. The cylindrical chamber has an inside diameter of 20.75 cm and a height of 37.46 cm from the bottom plate to the quartz plate, which seals the top of the chamber. The thickness of the quartz plate is 2.54 cm. A planar spiral induction coil is used to couple 13.56 MHz rf power into the plasma through an automatic impedance matching network to match the circuit to the 50 Ω rf source. The capacitive coupling to the plasma is minimized by introducing a Faraday shield between the antenna and the quartz plate.

Figure 2.4   The ICP system used in the experiment.

The vacuum system used in this set-up consists of the combination of two pumps:

a mechanical roughing pump and a turbo pump. The ultimate pressure achieved with this

pumping system is in the 10^{-7} Torr range. The system is equipped with four mass flow

controllers one each for hydrogen, argon, nitrogen, and methane. The working pressure can be adjusted by controlling the opening of a throttle valve through a pressure feedback system. If necessary, four different gases can be introduced into the chamber simultaneously.

The rf power indicated in this thesis is the net power measured at the power supply, including the loss in the transmission line and in the matching network. The power loss in the transmission line is less than 1% of the total power.

2.3.1 Impedance Matching Circuit

If the antenna is directly connected to the 13.56 MHz rf power source, the power transfer from the source to antenna would be inefficient because of impedance mismatch [2]. In the ICP device, there is an automatic impedance matching network which provides a reactance automatically adjusted for changing plasma load impedance. The most common configuration in an ICP is the "L-type matching network" consisting of a shunt capacitor which has susceptance $B = \omega C$ and a series inductor which has a reactance $X = \omega L$. The one used in this set-up is a commercial system (Match Pro CPM-1000, Comdel, Inc.) comprised of a tuning unit and a control unit. The tuning unit contains the matching components (variable capacitors and inductors), two dc motor servos, and rf sensors to provide feedback to the dc motor servos. The control unit provides controls for manual and remote operation of the tuning unit.

2.3.2 Faraday Shield

In this set-up, the influence of the capacitive coupling is reduced by introducing a Faraday shield between the antenna and the quartz plate. The capacitive coupling present from the stray capacitance of the high powered antenna can be reduced to a minimum depending on the design of the shield. Figure 2.5 shows the induction coil and the

Faraday shield as viewed from the vacuum side of the quartz plate. The spoked Faraday shield is grounded by connecting the Faraday filter founding strap to the bottom of the matching network.

Induction coil
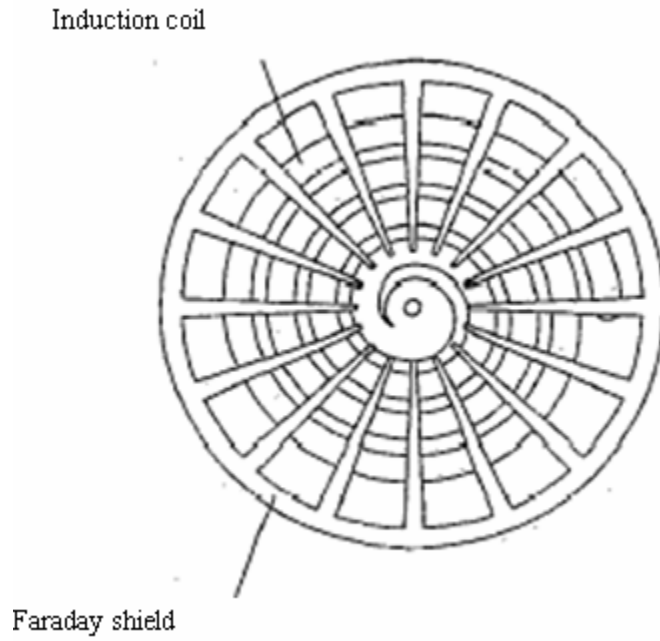
Faraday shield

Figure 2.5   Schematic Diagram of the Faraday shield and rf coil [21].

Chapter 3

Theoretical Background of Langmuir Probe Measurement

3.1 Principles of Langmuir Probe

Langmuir probe is widely used as basic diagnostics for characterization of low temperature plasmas that allow insertion of a small metal electrode (probe). The probe is biased and the current in the circuit is monitored as a function of the bias voltage. From the current-voltage ($I-V$) curve, the electron energy distribution function, electron temperature (if the energy distribution is Maxwellian), plasma space potential, and the floating potential can be deduced. In this section, the principle of the Langmuir probe is reviewed.

3.1.1 Sheath Formation in a Low Temperature Plasma

In the surface region of a vacuum chamber in which an rf plasma is produced, the plasma particles are lost to the chamber wall but the rf field replenish them and a charge neutral plasma is maintained. Electrons and ions must be lost to the chamber wall at the same rate to maintain charge neutrality (ambipolarity). Since the electron thermal speed is much higher than the ion thermal speed, electrons must be decelerated while ions must be accelerated towards the wall so that the fluxes of both species are the same,

$$n_i v_i = n_e v_e,$$
(3.1)

where $n_{i(e)}$ is the ion (electron) density and $v_{i(e)}$ is the ion (electron) average flow velocity. Sheaths, which are positive space charge regions, develop in front of the walls to maintain the aforementioned ambipolarity. A characteristic length related to the sheath is the Debye length, which is given by $\lambda_D = \sqrt{\varepsilon_0 kT_e / n_0 e^2}$ [44]. The sheath thickness is therefore of the order of the Debye length. Without a sheath, a plasma would be rapidly lost to the wall due to the lack of the electrostatic confinement.

The same sheath formation occurs when a Langmuir probe is inserted into a plasma. The Debye length is usually very short. For example, if $T_e = 1$ eV, $n_e = 10^{17} \, \text{m}^{-3}$, the Debye length is about 20 μ m. Therefore, in most practical cases, probe size far exceeds the Debye length which is the basic criterion for a conducting object to function as a Langmuir probe.

3.1.2 Mean Free Path

A general requirement for the application of Langmuir probe and the validity of Druyvesteyn formula is collisionless electron motion about the probe which requires that both the Debye length and probe diameter are much shorter than the electron mean free path. The mean free path of a particle in a medium is a measure of its probability of undergoing interactions of a given kind and is defined as the average distance that a particle (usually a molecule or atom) moves without colliding with something else. The mean free path for a particle with velocity v_{12}, moving through background particles with density n_2 is related to the cross-section corresponding to this type of interaction by the formula

$$\lambda_{12} = \frac{\langle v_1 \rangle}{n_2 \langle \sigma_{12} v_{12} \rangle},$$

(3.2)

v_{12} -relative velocity of particle 1 with respect to particle 2

σ_{12} -collision cross section between species 1 and 2

$<\sigma_{12}v_{12}>$ is the cross-section averaged over the velocity distribution, also called the

collision rate k_{12}.

In a plasma, the collisional processes that are the most likely to occur are elastic electron-neutral collisions, ion-neutral collisions and neutral-neutral collisions. The electron-neutral mean free path is taken as

$$\lambda_{en} = \frac{1}{N_g \sigma_{en}},$$
(3.3)

$$N_g = \frac{P}{kT_g},$$
(3.4)

N_g -density of neutral particles in the plasma in m^{-3}

P -gas pressure in Pa

T_g -temperature of neutral gas in K

σ_{en} -momentum transfer cross section for electron-neutral collisions

For hard-sphere collisions model

$$\sigma_{en} = \pi a_{12}^{2},$$
(3.5)

a_{12} -the distance between the center of masses of the two collision particles

For electron-neutral collisions, the electron radius is negligible in comparison with that of the atomic radius so that $a_{12} \approx a_{atom}$.

The electron-neutral collision mean free paths of argon plasma were calculated for a neutral gas having a temperature of 300 K according to Eq. (3.3) and the results are shown in Table 3.1.

P (mTorr)	1	10	50	500	1000
N_g (m^{-3})	3.216×10^{19}	3.216×10^{20}	1.608×10^{21}	1.608×10^{22}	3.216×10^{22}
λ_{en} (cm)	194	19.4	3.88	0.388	0.194

Table 3.1   Electron-neutral collision mean free path of Ar plasma at different gas pressure. The neutral gas temperature is assumed to be 300K.

From the data in Table 3.1, it can be seen that the electron mean free path is always larger than the largest probe radius that was used in ours experiment (0.375 mm). Actually, from the neutral gas temperature measurement by using OES, it is found that the gas temperature is always higher than 300 K, in the order of 1000 K. This may give a larger electron mean free path than the results calculated by assuming a neutral gas temperature of 300 K. So it is reasonable to use the collisionless sheath theory.

3.1.3   Langmuir Probe Current in a Plasma with Maxwellian Distribution

If the electron velocity distribution function is Maxwellian, a simple relationship between the Langmuir probe current and the bias voltage emerges. Let us consider a planar probe biased at a potential $V < 0$ relative to the plasma potential which is chosen to be 0. Since only those electrons having a velocity satisfying

$$\frac{1}{2}mv^2 > e|V|, \tag{3.6}$$

can be collected, the electron current is found to be

$$I = Sen_0 \sqrt{\frac{m}{2\pi T_e}} \int_{v_c}^{\infty} v \exp\left(-\frac{mv^2}{2T_e}\right) dv = I_{e0} \exp\left(\frac{eV}{T_e}\right) - I_{io}, \quad V < 0, \tag{3.7}$$

where S is the probe surface area, and v_c is the critical velocity given by

$$v_c = \sqrt{\frac{2e|V|}{m}}. \tag{3.8}$$

The electron saturation current is given by

$$I_{e0} = Sen_0 \sqrt{\frac{T_e}{2\pi m}}, \tag{3.9}$$

and the ion saturation current, which is governed by the sheath, is given by

$$I_{i0} = Sen_0 \sqrt{\frac{T_e}{eM}} = 0.605 Sen_0 \sqrt{\frac{T_e}{M}}. \tag{3.10}$$

(Note that the Bohm criterion requires that the ion velocity entering the sheath to be of the order of the ion acoustic speed. In Eq. (3.10), e is the electronic charge and e = 2.718⋯.) For a large negative probe potential, all the electrons are repelled and the ions collected. The collected current is $I = I_{io}$. The electron temperature can be obtained by taking the logarithm of the probe current, which can be represented by a straight line with the slope being proportional to $1/T_e$.

For a potential above the plasma potential ($V > 0$), all electrons are collected and the probe current becomes constant $I = I_{e0}$. The probe current vanishes at a potential $V = V_f$, with V_f the floating potential.
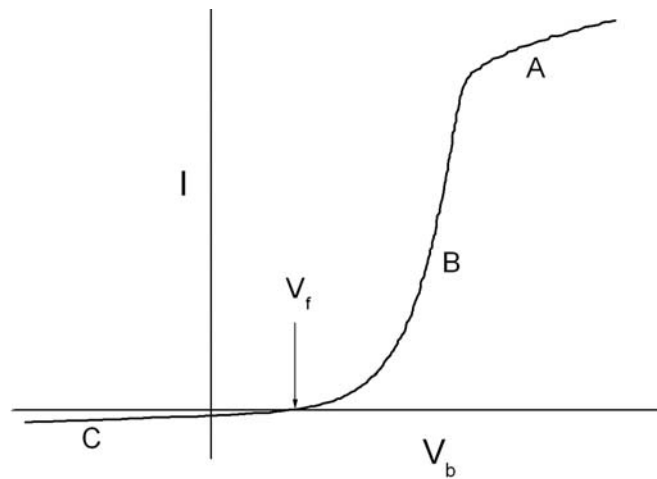
Figure 3.1   The Langmuir probe current as a function of the probe voltage.

21

3.1.4 Non-Maxwellian Probe Current

When the electron velocity distribution is not Maxwellian but still isotropic, and the mean free path λ_{mfp} of electrons is large compared to the probe dimensions, the Langmuir probe still applies and the probe current can be calculated as follows [45]. We assume that the probe collects electrons having a velocity component $v_z = v\cos\theta$, where v is the magnitude of the velocity and θ is the angle between the normal of the probe surface and the velocity of the collected electrons. Since the distribution function is isotropic by assumption, the current density becomes

$$I_e = eS\int f(\mathbf{v})\mathbf{v}\cdot\mathbf{n}d^3\mathbf{v}$$

$$= eS\int f(v,\theta,\varphi)v\cos(\theta)\sin(\theta)v^2dvd\theta d\varphi$$

$$= 2\pi eS\int_{v_{min}}^{\infty}\int_{0}^{\theta_{max}} v^3 f(v)\cos(\theta)\sin(\theta)dvd\theta, \tag{3.11}$$

where $\mathbf{v}$ is the velocity vector, $v = |\mathbf{v}|$ is the magnitude, and $f(v)$ is the electron velocity distribution function. Here, the minimum velocity of the electrons collected by the probe is

$$v_{min} = \sqrt{\frac{2e}{m}\left(V_p - V_b\right)}, \tag{3.12}$$

and

$$\theta_{max} = \cos^{-1}\left(\frac{v_{min}}{v}\right). \tag{3.13}$$

For an isotropic distribution, the distribution function is a function of energy $\varepsilon = \frac{1}{2}mv^2$, and thus

$$n_e = 4\pi \int v^2 f(v) dv = 4\pi \sqrt{\frac{2}{m^3}} \int f(\varepsilon)\sqrt{\varepsilon} d\varepsilon = \int f_E(\varepsilon) d\varepsilon, \qquad (3.14)$$

where $f_E(\varepsilon)$ is the electron energy distribution function (EEDF) given by

$$f_E(\varepsilon) = 4\pi \sqrt{\frac{2}{m^3}} \sqrt{\varepsilon} f(\varepsilon). \qquad (3.15)$$

$f(\varepsilon)$ is called the electron energy probability function (EEPF).

Integration of Eq. (3.11) over θ results in

$$I_e = \pi e S \int_{v_{\min}}^{\infty} v^3 f(v)(1 - \frac{2e(V_p - V_b)}{mv^2}) dv$$

$$= \frac{2\pi e S}{m^2} \int_{e(V_p - V_b)}^{\infty} f(\varepsilon)(\varepsilon - e(V_p - V_b)) d\varepsilon. \qquad (3.16)$$

If we define $V = V_p - V_b$ and $A = \dfrac{2\pi e S}{m^2}$

The first derivative of I_e with respect to V yields

$$\frac{1}{Ae}\frac{dI_e}{dV} = \int_{eV}^{\infty} \frac{\partial}{e\partial V}[f(\varepsilon)(\varepsilon - eV)] d\varepsilon$$

$$= -\int_{eV}^{\infty} f(\varepsilon) d\varepsilon. \qquad (3.17)$$

The second derivative of I_e with respect to V yields the Druyvesteyn formula which

provides a measure of evaluating the EEDF.

$$\frac{d^2 I_e}{dV^2} = Ae^2 f(eV) = Ae^2 f(\varepsilon). \qquad (3.18)$$

Therefore, the relationship between the second order derivatives of the Current-Voltage

(I-V) curve and EEDF can be established:

$$\frac{d^2 I_e}{dV^2} \propto \frac{f_E(\varepsilon)}{\sqrt{\varepsilon}} \propto f(\varepsilon). \qquad (3.19)$$

Equation (3.18) is applicable to an arbitrary distribution function as long as it is isotropic.

23

3.2 Measurement Method

A number of methods have been developed for obtaining differentiated probe characteristics [46]. The simplest method involves graphical differentiation of the characteristic in the electron-retarding region. It is, however, subject to considerable error.

As an alternative, the coupling of accurate phase sensitive detection and digital data acquisition and analysis, with the harmonic differentiation technique may prove useful under certain plasma environments where active differentiation is untenable. The phase sensitive detection has been used for the acquisition of the second derivative of the I-V characteristic [39, 40]. The method is based on superimposing a small ac potential on the dc probe bias, and then utilizing the nonlinearity of the probe current-voltage characteristics to obtain derivative information related to the harmonic distortion of the ac signal. When a small ac signal with a frequency ω is added to the dc probe bias,

$$V_b(t) = V_b^0 + v_0 \sin(\omega t), \tag{3.20}$$

$$v_0 \ll V_b^0,$$

where V_b^0 is the dc probe bias voltage and v_0 is the ac probe bias amplitude.

The corresponding probe current density J as a function of probe bias can be expressed in terms of a Taylor series about V_b^0,

$$J(V_b^0 + v_0 \sin(\omega t)) = J(V_b^0) + v_0 \sin(\omega t)J'(V_b^0) + \frac{v_0^2}{2}\sin^2(\omega t)J''(V_b^0) + \cdots \tag{3.21}$$

Expand sine terms

$$J = J(V_b^0) + \frac{v_0^2}{4}J''(V_b^0) + \frac{v_0^4}{64}J^{iv}(V_b^0) + \frac{v_0^6}{2304}J^{vi}(V_b^0) + \cdots$$

$$+[v_0 J'(V_b^0) + \frac{v_0^3}{8} J'''(V_b^0) + \frac{v_0^5}{192} J^{iv}(V_b^0) + \cdots]\sin(\omega t)$$

$$-[\frac{v_0^2}{4} J''(V_b^0) + \frac{v_0^4}{48} J^{iv}(V_b^0) + \frac{v_0^6}{1536} J^{vi}(V_b^0) + \cdots]\cos(2\omega t) + \cdots \qquad (3.22)$$

The leading term of the second harmonic is $\frac{v_0^2}{4} J''(V_b^0)\cos(2\omega t)$ and we get

$$J^{2\omega} \approx \frac{1}{4} v_0^2 \frac{d^2 J_e}{dV_b^2}\cos(2\omega t). \qquad (3.23)$$

Equation (3.23) expresses the generalized relation between the detected amplitude of the second harmonic signal and the second derivative of the prove I-V curve, which is connected to the EEDF through Eq. (3.19). In the experiment, the plasma potential V_p is assumed constant and $edV = edV_b = d\varepsilon$ according to Eq. (3.12). When V_b is scanned slowly, a complete EEPF curve can be obtained.

3.3   Maxwellian and Druyvesteyn Distribution

The electron energy distribution function in low pressure discharges may often be approximated by either Maxwellian or Druyvesteyn distribution. Physically, Maxwellian distribution function is realized when the electron collision frequency is velocity independent, while Druyvesteyn distribution prevails when the mean free path is velocity independent. To appreciate the qualitative difference between Maxwellian and Druyvesteyn distribution functions, the EEPFs of both types are shown in Fig. 3.2 with common average electron energy of 2.5 eV. The probability functions are normalized with the area under the curves being 1. The respective electron energy probability functions are given by

Maxwellian EEDF: $f_M(\varepsilon) = 0.52442\sqrt{\varepsilon}\exp\left(\dfrac{-1.5\varepsilon}{\langle\varepsilon\rangle}\right).$ (3.24)

Druyvesteyn EEDF: $f_D(\varepsilon) = 0.2642\sqrt{\varepsilon}\exp\left(-0.55(\dfrac{\varepsilon}{\langle\varepsilon\rangle})^2\right).$ (3.25)

For Maxwellian distribution, the average energy and temperature are well defined as

$$\langle\varepsilon\rangle = \frac{3}{2}T_e.$$ (3.26)
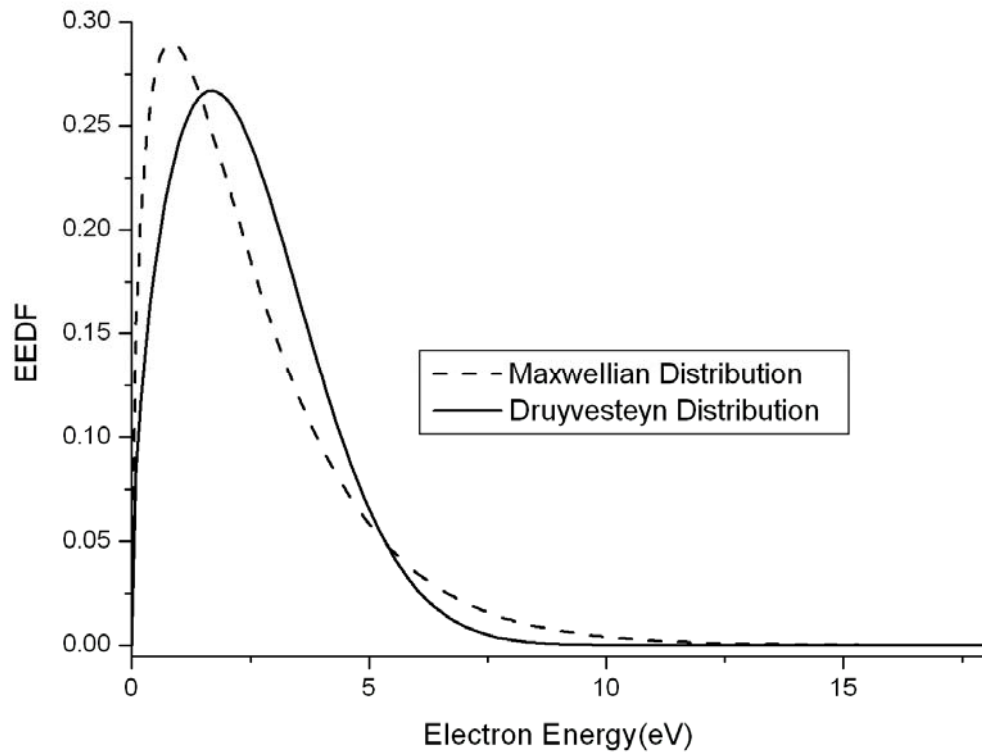
Figure 3.2   Druyvesteyn and Maxwellian electron energy probability function with the same average electron energy of 2.5 eV.

In comparison with Maxwellian distribution, Druveysteyn distribution is characterized by depletion in the high energy region and a shift of the maximum towards a higher energy.

3.4   Probe Circuit Used in Experiment

Two radially movable Langmuir probes made of tungsten have been used to measure the plasma parameters along a radius of the plasma. One of the probe tip used is a tungsten wire of radius 0.325 mm and length 2.2 mm covered by an alumina ceramic tube. The alumina tube is mounted on a stainless steel tube inserted in the chamber using a movable Wilson vacuum seal. Another probe used to measure the probe I-V curve has a similar structure as the first one. The only difference is with a probe tip of 0.25 mm radius. The construction of the probe is shown in Fig. 3.3.
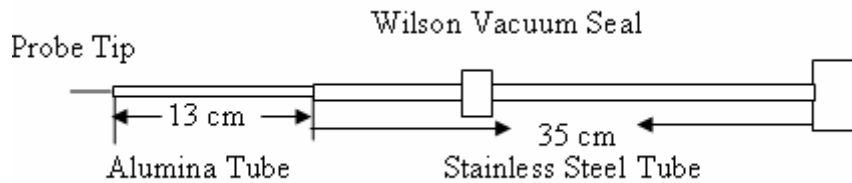
Figure 3.3   The Langmuir probe and support.

The Langmuir probe measuring circuit is shown in Fig.3.3. A saw-tooth wave with a frequency around 1 Hz was fed into the bipolar operational power amplifier (Kepco) from a 3010 function generator (Dynascan Corporation) before going to the probe and was recorded by an analog to digital converter (ADC) IBM data acquisition card with a resolution of 12 bits and stored by a computer. The sinusoidal wave generator provided a 50 KHz ac signal with an amplitude of 1 V. But the signal coupled, through the transformer, to the probe tip was below 50 mV. The signal was processed by a frequency doubler. A lock-in amplifier was used to filter the noise and measure the

27

magnitude of the 2ω component corresponding to the 2nd derivatives of the probe current, which was also recorded by the digital card and computer. The information on the Current-Voltage curve of the probe was obtained by measuring the voltage drop over the resistor.
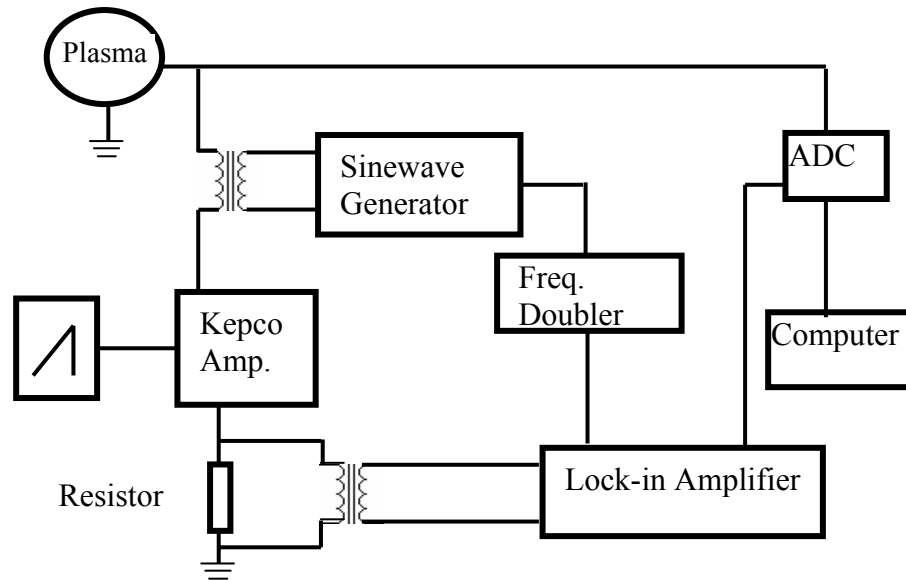
Figure 3.4   Probe circuit used in the experiment for EEDF measurement.

Chapter 4

Results of Electron Energy Probability Function measurements

4.1 EEPF in Argon Discharges

4.1.1 Results of EEPF Measurements in Argon ICP

Measurements reported in this section were made in argon discharge with pressures varying from 1 to 900 mTorr and the discharge powers in the range of 100-600 W. The probe is at the position of $r = 2.3$ cm, and $z = 28.7$ cm from the bottom of the chamber. No account is taken of the ion current since the contribution of the ion flux to the total current is negligible [19, 20]. The probe is cleaned by applying a high positive voltage until it glows red before each scan.

The effect of gas pressure on EEPF at 100 W rf power is shown in Fig. 4.1. The EEPF at 1 mTorr is close to a Maxwellian distribution below 11.6 eV, which is the first excitation energy of argon. The high energy tail is depleted compared with the low energy part and this can be seen clearly from Fig. 4.2. The EEPF can be described as a two-temperature distribution with the electron temperatures of T_{e1} and T_{e2}, which are

defined as $\dfrac{-1}{d(\ln(f(\varepsilon))/d\varepsilon}$. When the pressure reaches 10 mTorr or above, the EEPF

becomes more Druyvesteyn like than Maxwellian since the logarithm of EEPF is approximately proportional to ε^2 as shown in Fig. 4.3.
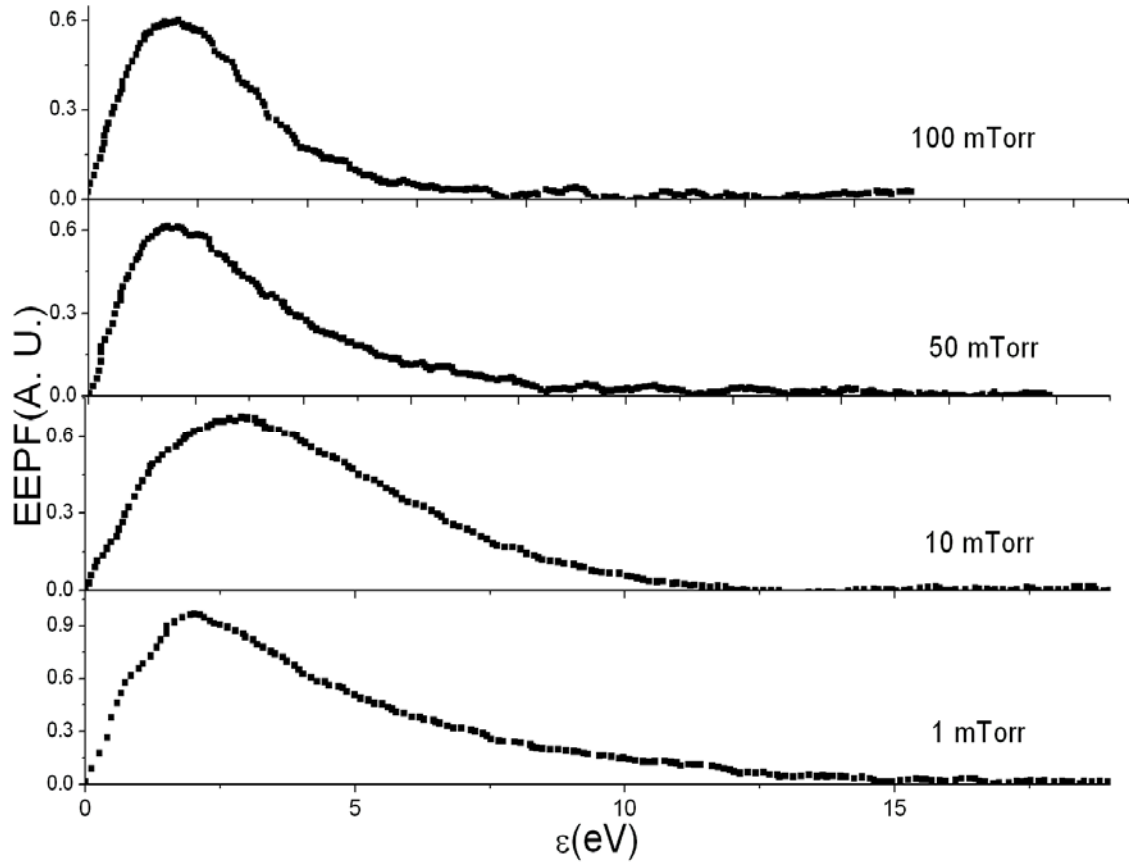
Figure 4.1   Evolution of EEPFs with gas pressure at 100 W, $r = 2.3$ cm, $z = 28.7$ cm.
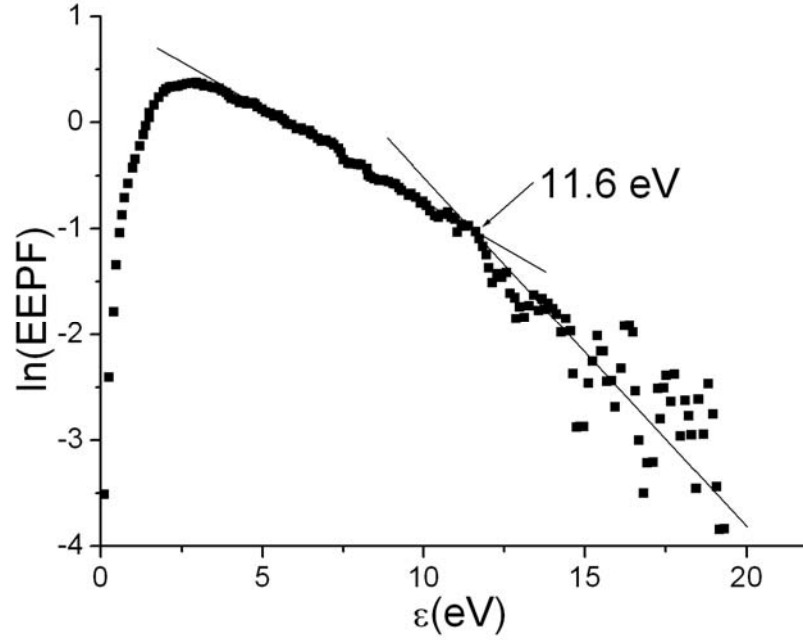
Figure 4.2   ln(EEPF) at 1 mTorr, 100 W. Example of two-temperature Maxwellian distribution.
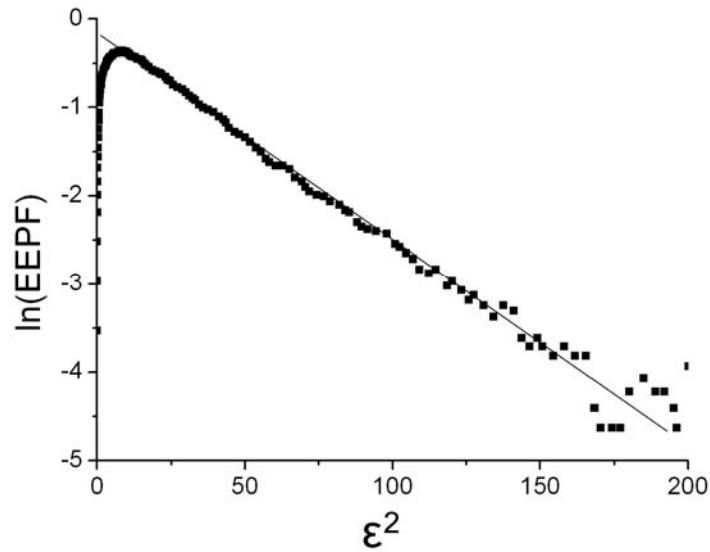
Figure 4.3   ln(EEPF) vs. ε^2 at 10 mTorr 100 W. Example of Druyvesteyn distribution function.

The EEPFs have also been multiplied by $\varepsilon^{1/2}$ to get the EEDF and then fitted with function in the form $A\varepsilon^{1/2} \exp[-(\varepsilon/B)^r]$, where A, B and r are fitting parameters. The

31

Maxwellian electron energy distribution corresponds to $r = 1$ and the Druyvesteyn distribution corresponds to $r = 2$. The results are shown in Fig. 4.4 in term of the logarithm of gas pressure. It is seen that the power r increases with the pressure from 1.3 at 1 mTorr to 2.2 at 10 mTorr or above implying which implies that the EEDF becomes more Druyvesteyn like as the pressure is increased. This result is consistent with that shown in Fig. 4.1-4.3. At a fixed pressure of 1 mTorr, the parameter r increases with the discharge power as well, which also implies a transition to Druyvesteyn distribution. All the results shown in Fig. 4.4 were averaged over three different sets of data acquired under the same discharge condition. The experimental errors are estimated to be around 15% by calculating $(r - \bar{r})/\bar{r}$, where $\bar{r}$ is the average of the fitting power.
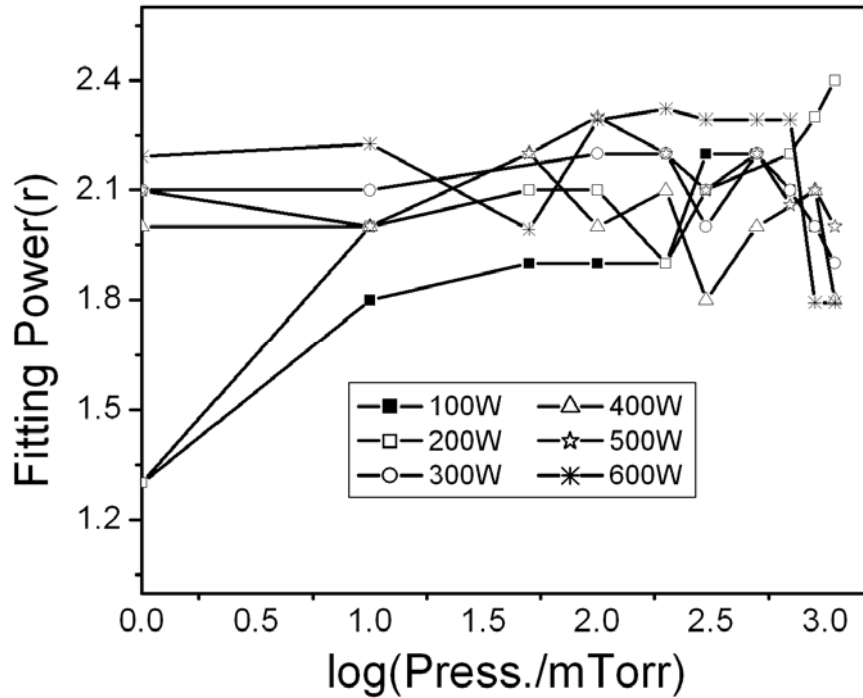
Figure 4.4   Fitting power r vs log(Pressure/mTorr) at different discharge power.

One of the possible reasons for the departure from a Maxwellian distribution at 1 mTorr is the localization of power deposition in ICP and the insufficient electron-electron collisions due to the low electron density in low-pressure plasmas. In ICP, most of the power deposition occurs at the place where the inductive electric field is high. This field is not distributed over the whole plasma but has a ring shape, centered on the chamber axis [47]. As a result, different energy groups are formed as electrons that pass through the high electric field region can obtain energy while electrons in other low electric field region can not get this energy [48]. Another factor that may affect the high energy electron depletion might be the rapid loss of high energy electrons through diffusion to the wall and recombination at the wall [49].

Druyvesteyn distribution is typical for the argon plasma in dc or low-frequency fields with negligible electron-electron collisions [50, 51]. In the high electron density inductively coupled plasma, this deviation from a Maxwellian and approach to Druyvesteyn distribution at higher gas pressures can be attributed to the ohmic heating or collisional heating that dominates the formation of EEPF at a high pressure. This can be seen from the electron energy diffusion coefficient D_ε, which contains all the information about the electron heating process. The EEPF formation is determined by $n_e D_\varepsilon$ [52]. In an inductively coupled plasma, D_ε takes the form of

$$D_\varepsilon = \frac{e^2 \varepsilon}{2 m_e \omega} \sum_{m,n} J_2^2(\alpha_{1m}) |E_{mn}|^2 \, \Theta\left(\frac{q_n v}{\omega}, \frac{v}{\omega}\right),$$

(4.1)

where a_{1m} is the m-th zero of the first order Bessel function, E_{mn} is the Fourier-Bessel component of the inductive field, ω is the rf frequency and $\Theta\left(\frac{q_n v}{\omega}, \frac{v}{\omega}\right)$ represents the

interaction between an electron with thermal velocity v and the electric field component E_{mn} [15].

The quantity $n_e D_\varepsilon$ in the low energy region of less than 10 eV increases with the pressure. In the high pressure regime where the electron neutral collision frequency is higher than the rf frequency, $\Theta\left(\dfrac{q_n v}{\omega}, \dfrac{v}{\omega}\right) \approx \dfrac{\omega}{v}$, and D_ε is proportional to $\dfrac{1}{v}$. Thus the energy transfer is strongly dependent on the variation of the momentum transfer cross section. Due to the Ramseur effect in the collisions between neutrals and electrons, low-energy electrons can be effectively heated by the electric field. Furthermore, the low energy electrons can interact with the electric field with longer time and more efficiently obtain energy from the rf electric field. As a result, the transition to Druyvesteyn distribution occurs due to the heating of the low energy electrons. The transition to the Druyvesteyn distribution is expected to occur at the condition where $\dfrac{\omega}{v} \ll 1$ [15]. The comparison between the rf frequency and v calculated from the measured plasma parameters is presented in Fig. 4.5 It serves to show that, the momentum transfer frequency of argon plasma is smaller than the rf frequency at 1 mTorr. As the pressure rises to 10 mTorr or above, $\dfrac{\omega}{v} < 1$. The transition of the EEPF to a Druyvesteyn distribution is thus expected to occur at this pressure.
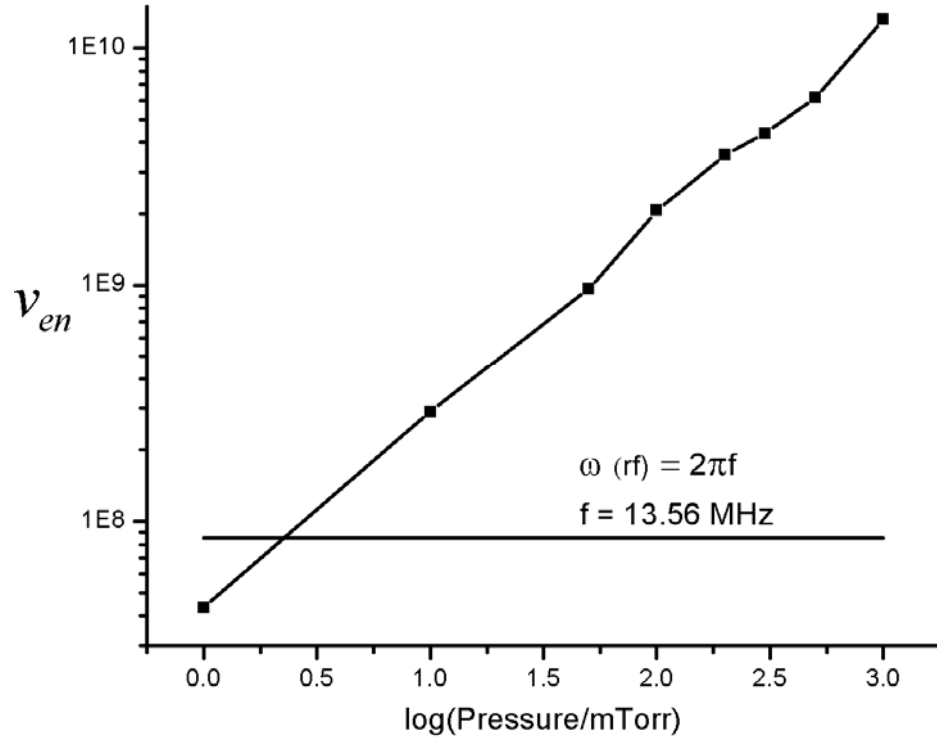
Figure 4.5   Comparison between the momentum transfer and rf frequency.

The approach to a Druyvesteyn distribution of the EEPF at higher gas pressure has also been observed by Gudmundsson *et al.* [13] in an oxygen/argon planar inductive discharge and by Michael S. Barnes *et al.* [14] in a planar inductive oxygen rf glow discharge, in which the distribution functions ranging from Maxwellian at 0.5 mTorr to almost Druyvesteyn-like at 10 mTorr were reported.

In this study, the EEPF is also found to shift to Druyvesteyn distribution with increasing rf power. This phenomenon might be caused by the large probe circuit resistance which tends to distort the EEPF especially when the probe circuit resistance is larger than or comparable to the probe sheath differential resistance, $R = (dI / dV_b)^{-1} \approx (kT_e / e) / I_{e0}$, which becomes smaller when the electron saturation

current is large. In order to solve this problem, a special probe circuit with a small resistance needs to be designed.

4.1.2   Radial Dependence of EEPFs in Argon Discharges

Figure 4.6 depicts the radial dependence of the measured EEPF taken at $z = 28.7$ cm and selected r values varying from 2.3 to 10.2 cm, under the discharge condition of 1 mTorr pressure and 100 W rf power. The average electron energy taken at different radial position has been evaluated and it varies by 4% at 1 mTorr as shown in Table 4.1, The small variation of the average electron energy indicates that the radial dependence of the EEPF is weak. But, when the pressure reaches 50 mTorr, the radial variation of $\langle \varepsilon \rangle$ becomes up to 14.5% and the assumption of the spatial independence of EEPF may not be valid at the high pressures. The significant variation of the $\langle \varepsilon \rangle$ can be seen from Table 4.2.

	100W	200W	300W	400W
r=2.3cm	4.40eV	4.87eV	5.56eV	6.35eV
r=4.8cm	4.29eV	4.83eV	5.49eV	5.93eV
r=7.4cm	4.60eV	4.80eV	5.73eV	5.87eV
r=10.2cm	4.45eV	4.63eV	5.40eV	5.89eV
ε_{ave}	4.44eV	4.78eV	5.55eV	6.01eV
δ_{max}	3.60%	3.10%	3.20%	4.00%

Table 4.1   Radial variation of the average electron energy, its radial average and maximum deviation δ_{max} at 1 mTorr.

	100W	200W	300W	400W
r=2.3cm	2.19eV	1.95eV	1.87eV	1.83eV
r=4.8cm	2.11eV	1.95eV	1.94eV	1.80eV
r=7.4cm	2.07eV	1.67eV	1.73eV	1.67eV
r=10.2cm	1.83eV	1.53eV	1.59eV	1.53eV
ε_{ave}	2.05eV	1.79eV	1.78eV	1.71eV
δ_{max}	10.70%	14.50%	10.70%	10.50%

Table 4.2   Same as Table 4.1 at 50 mTorr.

The spatial independence at a low pressure may be attributed to the non-local property of the electrons in a plasma. In low pressure gas discharges, the electrons diffuse over a long distance before their energy changes because the inelastic collisions occur at a rather low frequency. The large electron mean free path and low frequency inelastic collisions give rise to so-called non-local effect influencing the EEPF. The spatially homogenous EEPF and the applicability of non-local theory in an argon ICP discharge have been verified by Kortshagen *et al*. [22]. Similar result has also been reported by Singh *et al.* [24] and Mumken [53]. These authors have revealed that the applicability of non-local property became invalid with the increasing gas pressure. Mahoney *et al* [21] revealed that there was significant spatial variation in the form of the EEDFs at 10 mTorr and this variation became insignificant when the pressure reaches 50 mTorr.

In this study, it has been found that the validity of non-local behavior holds when the pressure is lower than 10 mTorr.
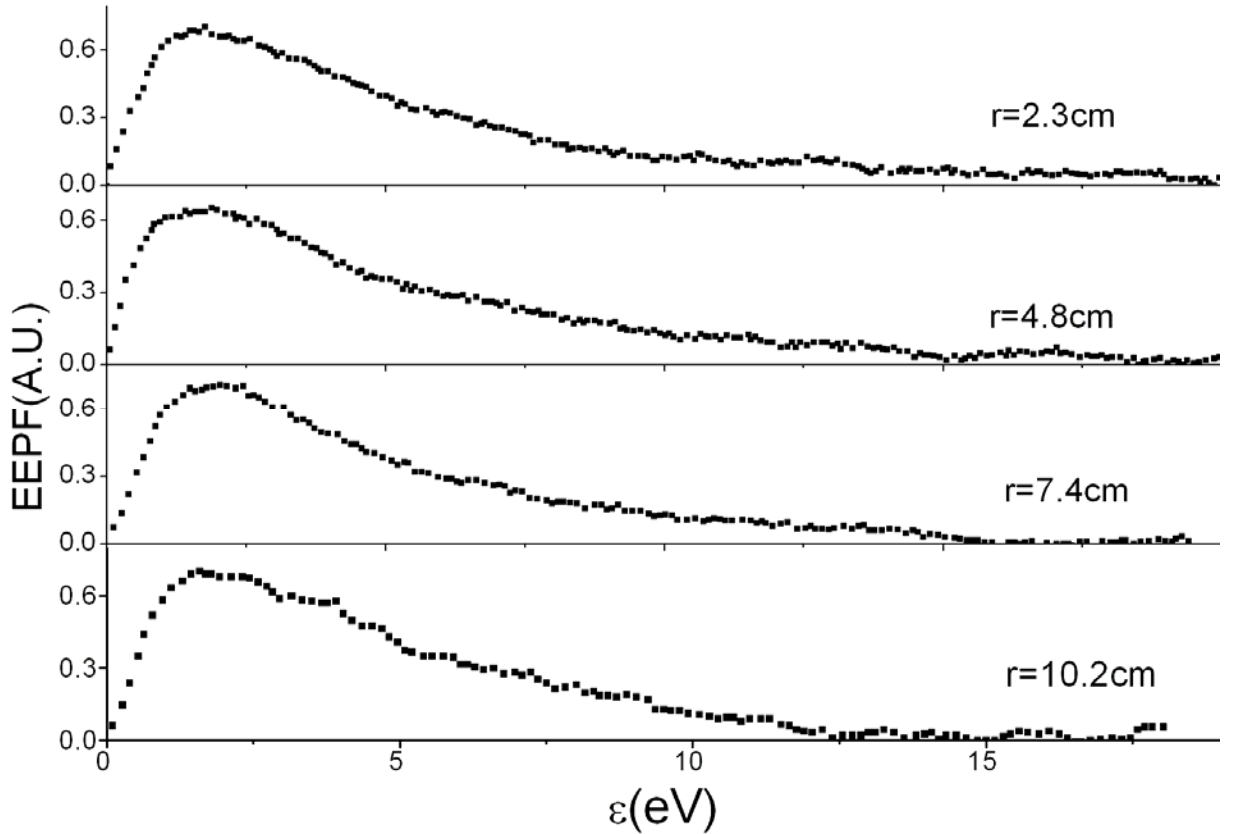
Figure 4.6   Radial variation of EEPFs at 1 mTorr 100 W.

4.2 Nitrogen and Hydrogen Discharges

EEPFs in nitrogen and hydrogen discharges have been found to be neither Maxwellian nor Druyvesteyn under the discharge conditions investigated. Figures 4.7 and 4.8 show the effect of discharge power on EEPF in a nitrogen discharge at 5 mTorr and 100 mTorr working pressure respectively. An extra peak in the EEPF is observed under all the discharge conditions that have been investigated.
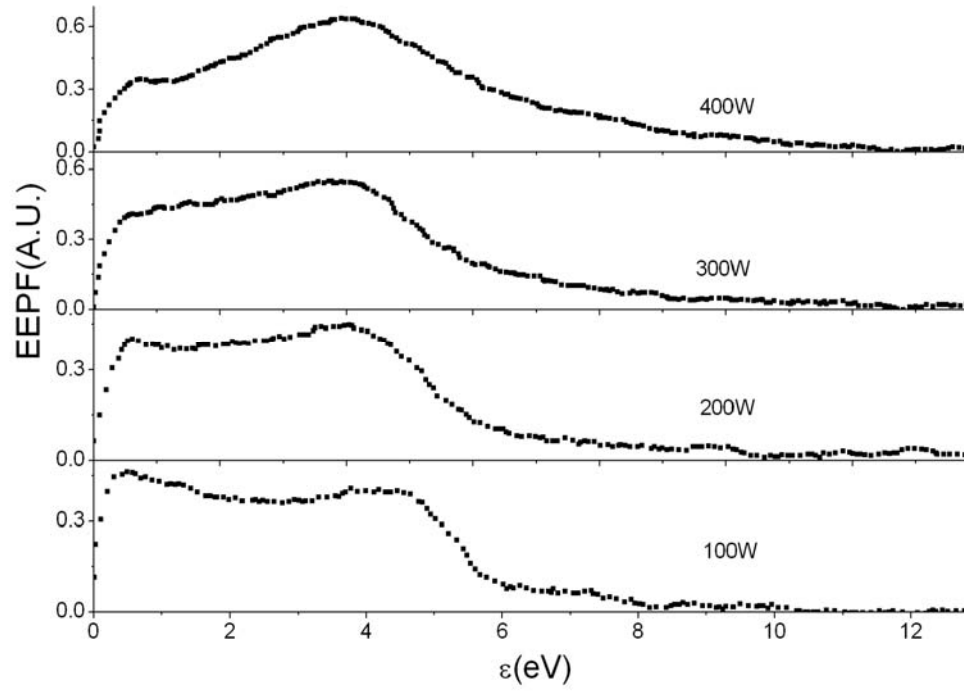
Figure 4.7   EEPFs in nitrogen plasma at 5 mTorr and different discharge powers.
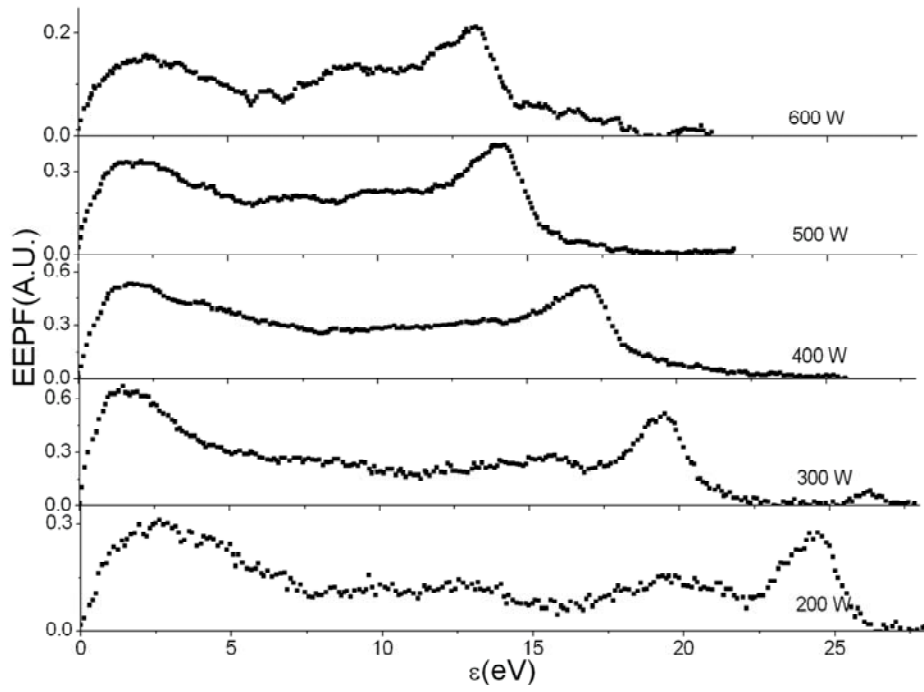
Figure 4.8   EEPFs in nitrogen plasma at 100 mTorr and different discharge powers.

The position of the second peak varies for different discharge conditions and ranges from around 3.5 eV at 3 mTorr to 24.0 eV when the pressure reaches 100 mTorr. Generally, it shifts to higher energies with the rise of working pressure whereas to lower energies when the discharge power is increased. The effect of discharge power becomes more significant when the gas pressure reaches 50 mTorr and higher.

The effect of gas pressure between 5-50 mTorr over the discharge power range of 100-600 W has also been investigated in the hydrogen discharge. No other data beyond this range has been acquired due to the limit of the device. The measured EEPF in hydrogen plasma has a structure similar to that in the nitrogen plasma and there are two peaks in the EEPF under most of the discharge conditions. The amplitude of the first peak decreases as the discharge power increases. The position of the second peak moves to the low energy direction when the discharge power is increased but to the high-energy direction when the gas pressure is raised.

This result is quite different from what has been reported by Singh *et al.* [24], who demonstrated that the molecular gases exhibit a nearly Maxwellian distribution at low pressures (between 10 and 30 mTorr) while the EEDF of the argon plasma is non-Maxwellian in this range by using a tuned, cylindrical Langmuir probe. At pressures above 30 mTorr, the electron energy distribution shows deviation from a Maxwellian distribution. It has also been pointed out that, in the nitrogen discharge, a hole in the EEPF is observed around 3 eV due to the presence of resonant electron-molecule vibrational excitation cross sections at 100 mTorr and the hole vanishes with increasing argon dilution [24].

For the results presented in this work, there are always two peaks in the measured EEPF under all the discharge conditions investigated. This phenomenon is more obvious at a high pressure but low discharge power because under these conditions, the local electric field (E/N, N is the neutral number density) that sustains the discharge might be small and the super-elastic collisions (a collision in which the translational energy of the fast-moving collision particle is increased) play an important role in the formation of the EEPF. In the ICP, the possible super-elastic collisions include the collisions between electrons and electronically or vibrationally excited molecules. As a result, super-elastic collisions involving vibrationally excited molecules are able to thermalize the EEPF at the vibrational temperature of the molecules, whereas the collisions involving electronically excited state produce a highly structured EEPF due to the heating of cold electrons by the excited states [54-56]. The energy gained by the electrons through collisions with the vibrational or electronically excited states may produce an extra peak in the EEPF as a result of the following reaction

$$e(\varepsilon) + A^* \rightarrow A^{*'} + e(\varepsilon + \Delta\varepsilon) \tag{4.2}$$
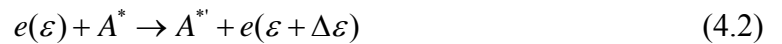
4.3 EEPF Measurement in Helium Discharges

In order to investigate whether the phenomenon of the extra peak in EEPFs of hydrogen and nitrogen plasmas is peculiar to the molecular gas or not, the EEPF measurement in the helium discharge was carried out. It is difficult to start a discharge in helium gas compared to the case of the argon because of the much higher ionization threshold energy of the helium gas. As the gas pressure decreases, it requires much more rf power to sustain the discharge and the minimum gas pressure for plasma production is found to be around 10 mTorr in this device.

The effect of gas pressure on EEPF at 200 W in the helium plasma is shown in

Fig. 4.9. The EEPFs in Fig. 4.9 show a transition from Maxwellian to Druyvesteyn

distribution as the pressure is increased. The transition is characterized by the depletion

of the high energy electrons in the distribution as pressure increases. Regarding the rf

power, there is a shift from Maxwellian to Druyvesteyn distribution at 20 mTorr when

the rf power is increased from 200 to 300 W.

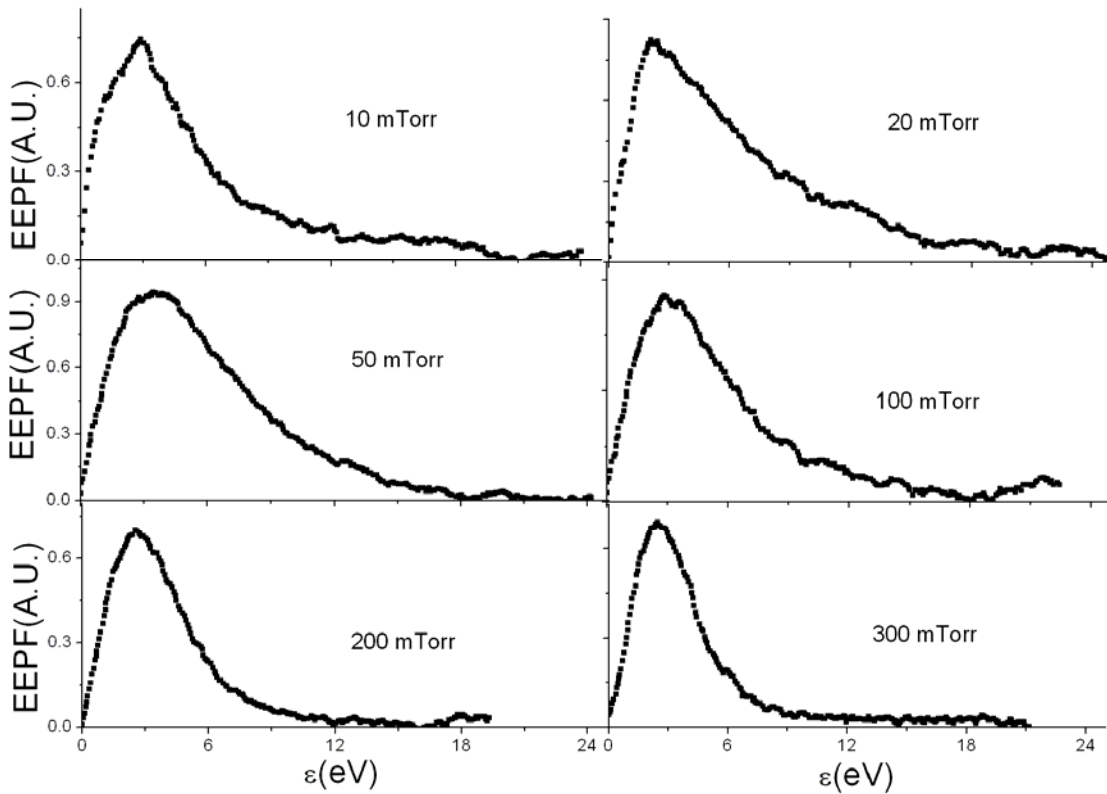Figure 4.9   EEPFs in helium discharges at fixed rf power of 200 W and different
pressures.

In conclusion, the EEPF of helium discharge also distinguishes from that of the

nitrogen and hydrogen significantly. No extra peak was found in the helium EEPF.

Comparisons between argon EEDF and helium EEDF in a capacitively coupled plasma

source has been made in reference [40]. It is reported that in the measured gas pressure

range in helium discharges, most electrons in the body of the EEDF have a Maxwellian distribution and T_{eff} falls with the increasing gas pressure. While in the argon plasma, there is a transition from Maxwellian to Druyvesteyn distribution. The difference was explained by the heating mode transition from stochastic heating to collisional heating in argon plasma. In this work, the EEPF in an inductively coupled plasma is found to show the transition to Druyvesteyn-like distribution as the pressure is increased in both the helium and argon discharges. It is believed that the colisional heating must also play an important role in the formation of the Druyvesteyn distribution in helium discharge.

4.4 Average Electron Energy and Density Measurements

4.4.1 Argon Plasma

Measurements of average electron energy $\langle \varepsilon \rangle$ and plasma density were made in the argon discharge for pressures from 1 mTorr to 1 Torr and input rf powers from 100 to 600 W. The average electron energy was calculated by

$$\langle \varepsilon \rangle = -1.5 \frac{1}{d \ln f(\varepsilon)/d\varepsilon}, \tag{4.3}$$

for Maxwellian EEPF, and for Druyvesteyn EEPF,

$$\langle \varepsilon \rangle = \sqrt{-0.55 \frac{1}{d \ln f(\varepsilon)/d(\varepsilon^2)}}. \tag{4.4}$$

The electron densities were calculated by either by Eq. (3.18) (Maxwellian distribution) or $n_e = I_e^* \sqrt{\dfrac{m_e}{2 < \varepsilon >}} \dfrac{1}{0.45 Se}$ (Druyvesteyn distribution) depending on the calculated average electron energy [57].

The variation of average electron energy with pressure and rf power is shown in Fig. 4.10. There seems to be no strong dependence of $\langle \varepsilon \rangle$ on the input rf power except at

a low gas pressure of 1 and 10 mTorr. It can be seen, however, that $\langle \varepsilon \rangle$ decreases sharply

for pressures lower than 50 mTorr.

The plasma density is found to be in the range of $10^{10} - 10^{12}$ cm^{-3}. Figure 4.11

shows the dependences of electron density on gas pressure and discharge power. The

density increases initially with increasing pressure. The density, however, peaks at

$P \approx 200\text{-}300$ mTorr and then decreases with the further increase of the pressure. The

discharge power also has a significant effect on the plasma density. Generally, a higher

discharge power leads to a higher electron density. At a high discharge power, the plasma

density increases by more than two orders of magnitude as the gas pressure increases

from 1 to 300 mTorr. From Fig. 4.12, it can be seen that there is a jump in the density

when the gas pressure rises from 10 to 50 mTorr. The densities increase linearly with the

logarithm of the gas pressure when the pressure is between 10 and 300 mTorr and the

effect of the power on the density is more significant at a high gas pressure but becomes

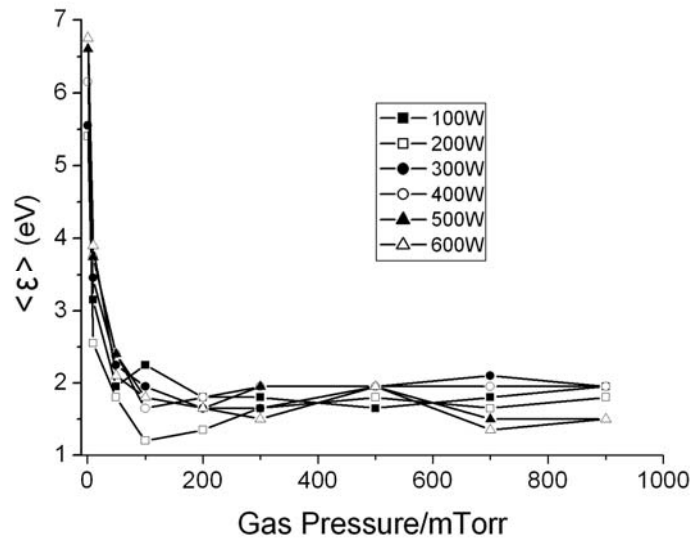insignificant at 1 mTorr.

Figure 4.10 $\langle \varepsilon \rangle$ as a function of the pressure at different discharge powers.
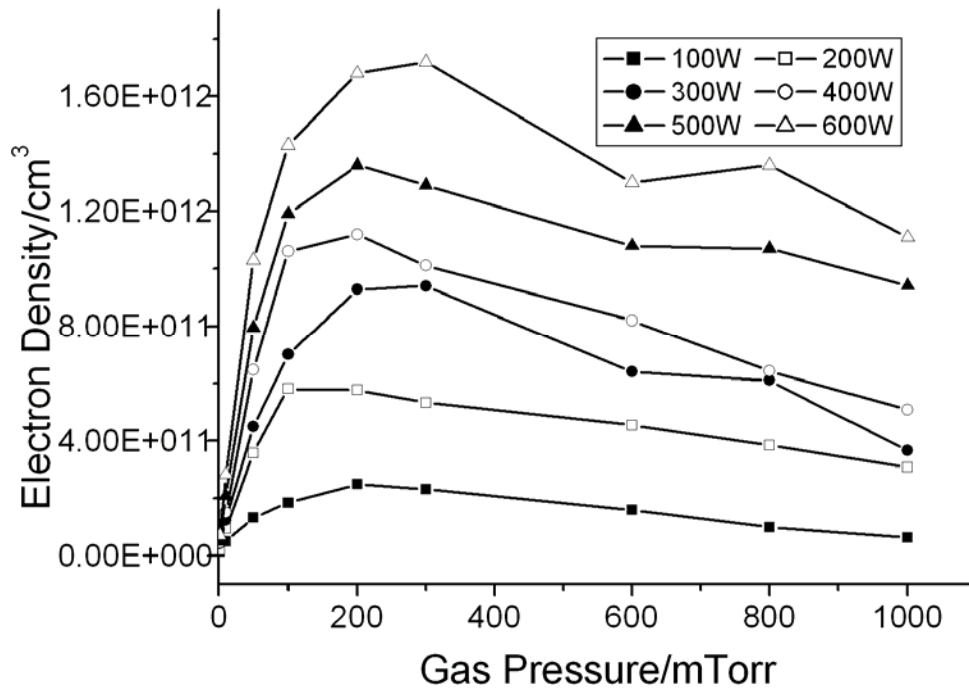
Figure 4.11 n_e-Pressure/mTorr at different discharge powers.
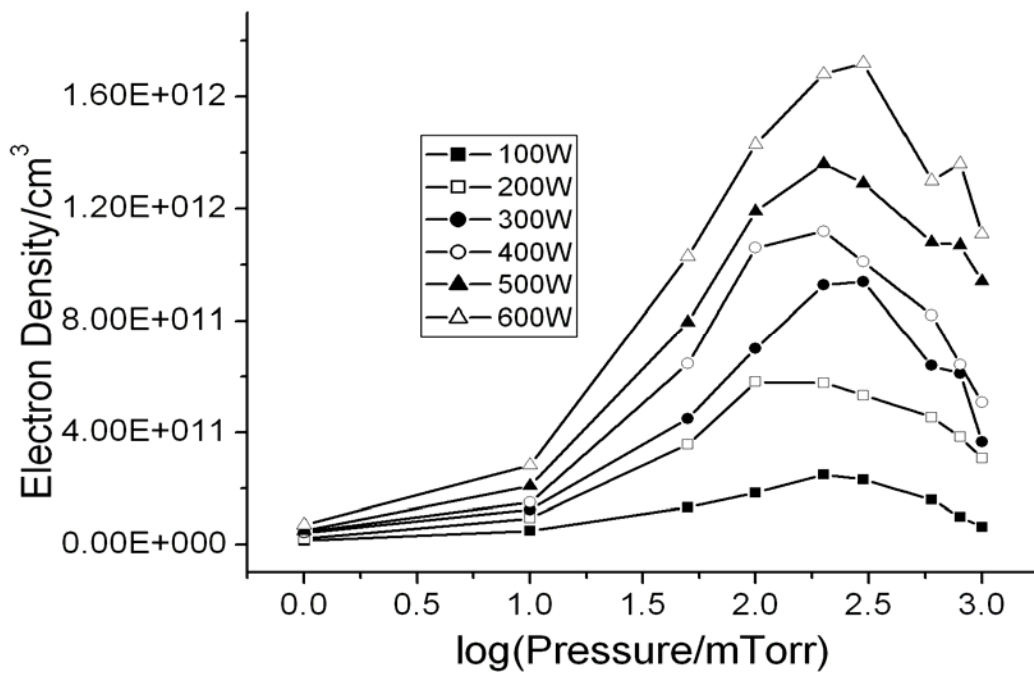
Figure 4.12 n_e vs. log(Pressure/mTorr) at different discharge powers.

The dependence of the average electron energy $\langle \varepsilon \rangle$ on gas pressure and rf power can be explained by the particle balance equation at the steady state due to the linear relationship between the effective electron temperature and $\langle \varepsilon \rangle$ [3]

$$\frac{K_{iz}(T_e)}{u_B(T_e)} = \frac{1}{N d_{eff}}$$

(4.5)

where $d_{eff} = \frac{1}{2} \frac{RL}{Rh_L + Lh_R}$ is the effective plasma size, R and L are the plasma source radius and length respectively, h_l and h_R are the edge to center density rations, $u_B(T_e)$ is the Bohm velocity, $K_{iz}(T_e)$ is the ionization reaction rate which can be approximated to be of Arrhenius type, $K_{iz} = K_{iz0} \exp(-E_{iz}/T_e)$, and N is the density of gas.

Since $u_B(T_e) = (kT_e/m_i)^{1/2}$, the ionization reaction rate increases more rapidly than u_B, the left side of Eq. (4.5) increases with an increase of the electron temperature, namely, the average electron energy. When the pressure is increased, the right side of Eq. (4.3) decreases and this implies a decrease of the electron temperature. It is also noted that, T_e is independent of input power. The main cause of the increase in $\langle \varepsilon \rangle$ with the increasing rf power at a low gas pressure is heating of the gas and the resulting decrease in the neutral number density [58].

The plasma density can be estimated from [3]

$$n_e = \frac{P_{abs}}{e u_B A_{eff} \varepsilon_L}$$

(4.4)

where $A_{eff} = 2\pi R(Rh_L + Lh_R)$ is the effective area for particle loss, $\varepsilon_L = \varepsilon_c + \varepsilon_e + \varepsilon_i$ is the total energy lost per ion from the system which contains collisional energy loss per ion-

electron pair (ε_c), and the energy transferred from the plasma to the chamber wall by ions (ε_i) and electrons (ε_e). Both ε_i and ε_e increase with the average electron energy. The collisional energy ε_c increases rapidly with increasing pressure in the high pressure regime as we can see from Fig. 4.13.
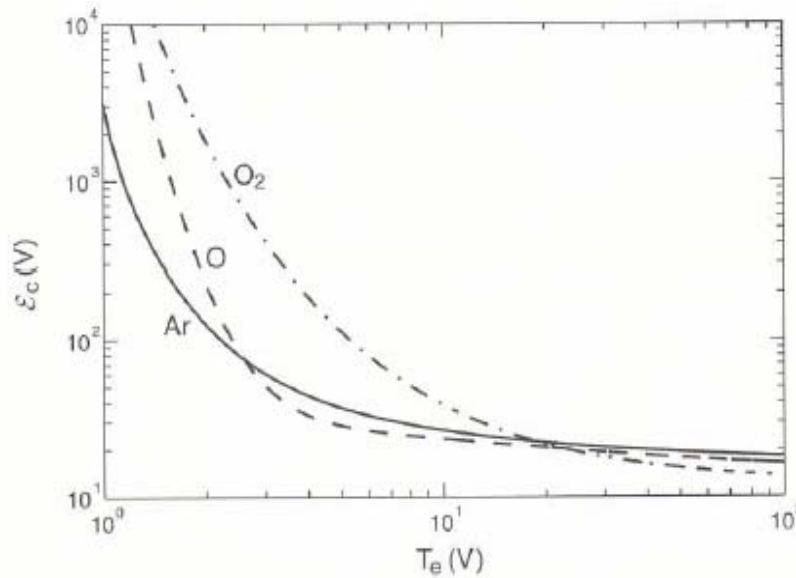
Figure 4.13   Collision energy loss per electron-ion pair created, ε_c vs T_e in argon and oxygen (Compiled by Gudmunsson, 2002 [3]).

In the low pressure range, the plasma density is dominated by the change in the diffusion energy loss, u_B, and A_{eff}. As a result, the plasma density increases when the gas pressure increases. In the high pressure range, the plasma density is dominated by the collisional energy loss and thus decreases as pressure is increased.

In this work, the electron density n_e depends on both pressure and input power and is peaked around 300 mTorr at a given rf power. The trends of the average electron energy and density on discharge power and pressure are similar to the normal trends observed in inductive discharge as reported in [59, 60]. The higher rate of inelastic

electron heavy particle collisions leads to the decrease of the $\langle \varepsilon \rangle$ with increasing pressure while the trend of n_e with increasing pressure is consistent with the power balance relation [60].

4.4.2 Helium Plasma

Figure 4.14 shows the calculated average electron energy in helium discharge as a function of gas pressure at rf powers of 200-600 W. The maximum average electron energy is as high as 10.0 eV under the discharge condition of 10 mTorr, 600 W. The average electron energy decreases as the working pressure increases due to the energy transfer from high-energy electrons to the neutrals. The dependence of the $\langle \varepsilon \rangle$ on rf power is insignificant. When compared with the argon discharge, usually, the average electron energy in helium discharge is higher than that of the argon discharge under the same discharge condition. This is reasonable because the ionization energy E_i of helium is larger than the E_i of argon [59].
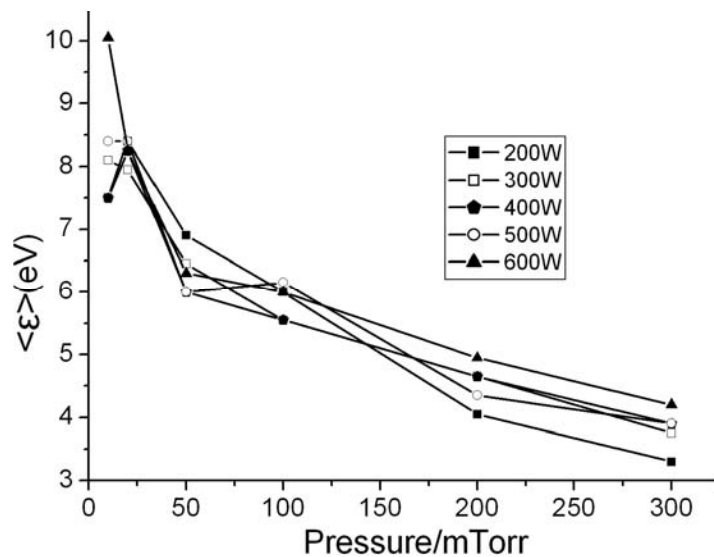
Figure 4.14 $\langle \varepsilon \rangle$ vs. pressure/mTorr at different discharge powers in helium plasma.

Chapter 5

Measurements of Neutral Temperatures in ICP

5.1 Introduction

It is generally assumed that in plasmas for materials processing, the neutrals are assumed to be at the room temperature. Nevertheless, the recent work on the neutral gas temperature measurement and modeling in the ICPs [25-36, 61-64] and some other devices [65, 66] has indicated that heating of neutral species is significant and gas temperatures in ICPs may exceed by a large margin the room temperature [25, 26].

Several methods have been developed to measure the neutral gas temperatures in ICPs. Hebner [29] used laser-induced fluorescence (LIF) in an Ar ICP and found that the neutral gas temperature reached 1000 K. Hebner and Miller [30] also measured radial distribution of the temperature of excited argon atoms Ar* in the same system. Temperatures in the range of 600-700 K were found in C_3F_6 inductively produced plasma at a pressure of 10 mTorr and an rf power of 200 W [31]. Singh *et al.* [32] used the ideal gas law to determine the gas temperatures from the total neutral gas density and deduced neutral temperatures in the range of 450-930 K. Abada *et al.* [33] measured the spatially and temporally resolved neutral gas temperature in a CF_4 planar inductive discharge using LIF and observed strong temperature gradients. The highest temperature reached 900 K in the reactor centre at a pressure of 50 mTorr and a power density of 0.15 W/cm^3.

The temperature increases with both gas pressure and power, but is independent of gas flow rate. Bol'shakov *et al.* [34] measured the gas temperature in ICPs by emission and diode laser absorption and observed a high temperature of 1285 K at 300 W in the pressure range of 300 mTorr. Gas temperatures on the order of 1400 K in a $Cl_2/BCl_3/N_2$ plasma at 1000 W rf power was reported by Donnelly and Malyshev [35]. In a plasma abatement device operated at 1200 W, temperatures as high as 2100 K were also reported [36]. The gas temperature as a function of gas pressure was also reported by Tonnis and Graves [26]. It has been found that the gas temperature is almost proportional to the logarithm of gas pressure. An increase in gas temperature with rf power was also found, but the dependence cannot be expressed by a simple analytical expression. Comparisons between molecular gas and atomic gas have also been made. It has been reported [26] that the molecular gas usually exhibits higher temperature under the same discharge condition compared with that of the atomic gases. The higher temperature of molecular gases may be attributed to Franck-Condon heating of neutral fragments during electron impact dissociation, vibrational excitation/thermalization, and exothermic wall reactions inside the molecular plasmas.

In this Chapter, results of neutral gas temperature measurements in a planar inductively coupled plasma based on optical emission spectroscopy previously proposed by Donnelly and Malyshev [25] will be presented. Both nitrogen and argon plasmas were studied. 5% nitrogen was added as an actinometer in the case of argon discharge.

5.2 Theoretical Description of Molecular Transition

Emission from molecules involves electronic (n), vibrational (v), and rotational (J) energy level transitions. For a diatomic molecule that the effect of electron spin

splitting and Λ doubling can be neglected, the total energy of the molecule can be expressed by

$$E = E_e + E_v + E_R$$

$$= hc\left(k_e + k_v + k_R\right).$$ (5.1)

where E_e, E_v, E_R represent the electronic energy, vibrational energy and rotational energy respectively, while k_e, k_v, k_R are the corresponding wave numbers. k_e can be obtained from most molecular spectroscopy handbooks. k_v is given by

$$k_v = \frac{1}{c}\left[\varpi_e(v+\frac{1}{2}) - \varpi_e x_e(v+\frac{1}{2})^2 + \varpi_e y_e(v+\frac{1}{2})^3 + \cdots\right],$$ (5.2)

where ϖ_e is electronic state dependent vibrational frequency, x_e, y_e are constants, and v is the vibrational quantum number ($v=0,1,2,\cdots$). Based on a vibrating symmetric top model, k_R is calculated as follows

$$k_R = B_v J(J+1) - D_v J^2(J+1)^2 + \cdots$$ (5.3)

where J is the rotational quantum number ($J=0, 1, 2,\cdots$). B_v is the rotational constant, and D_v is the distortional constant. Both constants are electronic state and vibrational state dependent.

For a transition from an upper state E' to a lower state E'', the total energy change is given by:

$$\Delta E = \Delta E_e + \Delta E_v + \Delta E_R.$$ (5.4)

ΔE_e, ΔE_v and ΔE_R correspond to the change of electric energy, vibrational energy and rotational energy, respectively. Expressed in the corresponding spectral terms, we can obtain the wavenumber of the transition

51

$$k = (k_e' + k_v' + k_R') - (k_e'' + k_v'' + k_R'')$$

$$= k_e + k_{v'v''} + k_R. \tag{5.5}$$

For a given system of band and vibrational state, k_e and $k_{v'v''}$ are both constants. So k can be expressed as

$$k = k_0 + k_R. \tag{5.6}$$

$$k_R = k_{R'} - k_{R''}. \tag{5.7}$$

The selection rules for this transition are

$$\Delta J = J' - J'' = -1, 0, 1, \tag{5.8}$$

except that $J'=0$ to $J''=0$ are forbidden.

The method used in this study to measure the neutral temperature was developed by Donnelly and Malyshev [25] and involved injection of small percentage of nitrogen gas (5% in our case) into an experimental gas and examining the spectrum of a molecular band. The molecular band is due to rovibronic transition from the upper $c^3 \prod_u$, $v'=0$, J' state to the lower $B^3 \prod_g$, $v''=0, J''$ state. Since v does not change, $\Delta G=0$ can be assumed. The selection rules for J' - J'' transition is $\Delta J = 0, \pm 1$, while 0-0 transitions are not allowed. Thus the molecular band can be split into three branches, P, Q, and R, corresponding to ΔJ being -1, 0, and 1, respectively. The lines of the tree branches combine to form a violet-degraded peak at 337.1 nm and broaden to lower wavelengths. This observed spectrum can then be modeled with the equation

$$I(J', J'') = aS(J', J'') \exp(-E(J') / kT_{rot}), \tag{5.9}$$

where the coefficient a is a proportionality constant dependent on the spectrometer sensitivity, rotational partition function and other factors. $S(J', J'')$ is the line strength

52

factor, which is approximated by $2J'+1$. $E(J')$ is the rotational energy at level J', given by

$$E(J') = hc[B_{v'}J'(J'+1) - D_{v'}J'^2(J'+1)^2],$$ (5.10)

where J' is the rotational quantum number of the upper state. k is the Boltzmann constant and T_{rot} is the rotational temperature of the upper state $C^3\prod_u$.

In order to synthesize a theoretical emission spectrum, we have calculated the wavelength and intensity factors using known rotational constants proposed by Herzberg [67]. In addition, the Gaussian type instrumental broadening has to be incorporated into the theoretical emission line intensity given by Equation (5.9) [68-70]. First, a Gaussian profile of each rotational emission line is calculated based on the measured instrumental broadening. Then, the intensity of each line falling into the predefined regular wavelength (or energy) bin is integrated. Finally, the intensities of all lines in that wavelength bin are summed up to form a synthesized spectrum. To compare an observed spectrum and the synthetic spectrum, the proportionality constant a in Equation (5.9) was adjusted so that the areas under the observed and synthetic spectra are equal. χ^2 (Chi-square) has been calculated for varying T_{rot} until a minimum χ^2 is found. The specific procedure is as follows:

(1) Convolution of the calculated line using the previously measured instrumental broadening function. A convolution is an integral that expresses the amount of overlap of one function g as it is shifted over another function f. It is also known as "folding". Convolution of two functions f and g over a finite range $[0, t]$ is given by

$$f * g = \int_0^t f(\tau)g(t-\tau)d\tau \qquad (5.11)$$

In our case, f represents the intensity of the spectrum at a specific wavelength and can be calculated from Equation 5.8 using the constants from Herzberg's book [67]. g is the Gaussian function

$$g = \frac{\sqrt{2}}{\sqrt{\pi}w}\exp\left(-\frac{2x^2}{w^2}\right), \qquad (5.12)$$

where w is the full width at half maximum (FWHM) and can be determined by measuring the spectrum from the calibrated Hg lamp. Each line is broadened after convolution with the instrumental profile. The integration is from minimum wavelength to the maximum wavelength of the target band, which is from about 330 nm to 339 nm in this calculation.

(2) The intensities were binned into regularly spaced wavelength increments. There are 90 bins for the full range of the wavelength from about 330 nm to 339nm. So the width of each bin is around 0.9 nm.

(3) The contribution from each line to each bin is summed to complete the computation of the synthetic spectrum.

(4) Subtract a linear background from the measured spectrum. This might be repeated for several times by subtracting a different constant from the spectrum to make sure that the background effect is limited to a minimum. Then fit the measured spectrum with the synthetic one at different temperature and find the T_{rot} with the smallest chi-square, which corresponds to the best fitting. The chi-square is calculated by the following equation

$$\chi^2 = P \frac{\sum\limits_{1}^{N}(x - x_0)^2}{N(N-1)}$$ (5.13)

P is the number of spectrum inside one bin divided by the total number of the spectrum, N is the total number of the bins, and x is the measured spectrum intensity while x_0 is the synthetic spectrum intensity corresponding to the same specific wavelength as x is.

The instrumental broadening function has been determined using the 436.2 nm Hg line. Figure 5.1 shows the experimental data and the best fit of a Gaussian profile. The circles represent the measured spectra and the solid line is the corresponding Gaussian fitting with a resolution of about 0.9 nm.
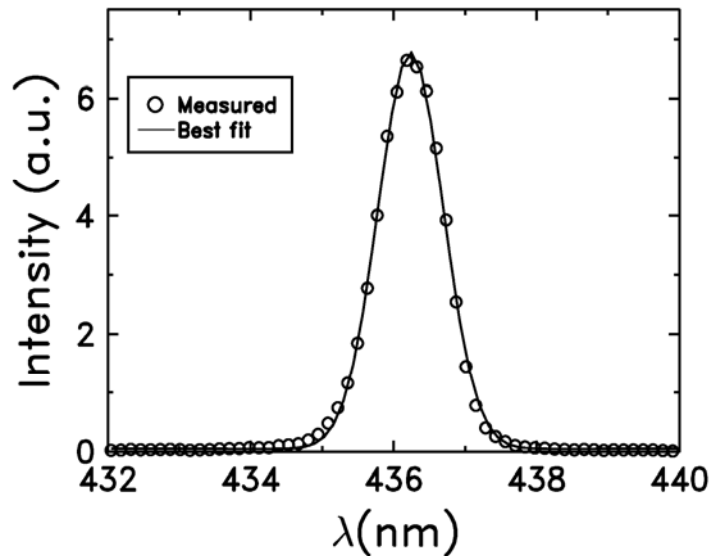
Figure 5.1   Instrumental function measured with 432.6 nm Hg line.

The synthetic spectrum without convolution with the instrumental function and the ones convoluted are shown in Figures 5.2 (a) and 5.1 (b), respectively. The instrumental function is taken from a calibrated Hg lamp and shows a Gaussian shape.
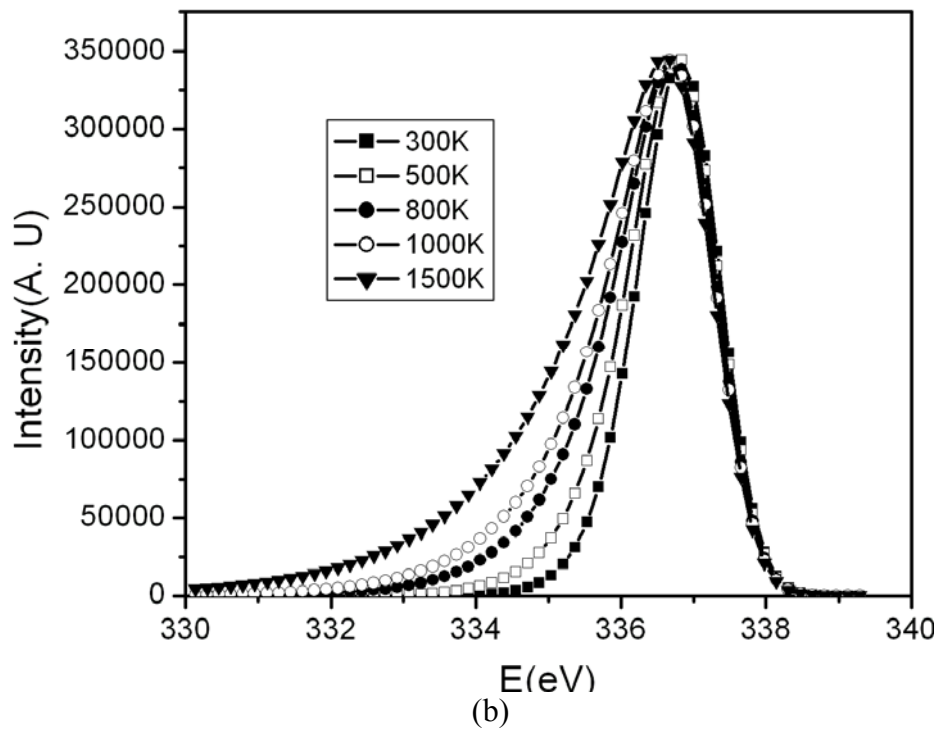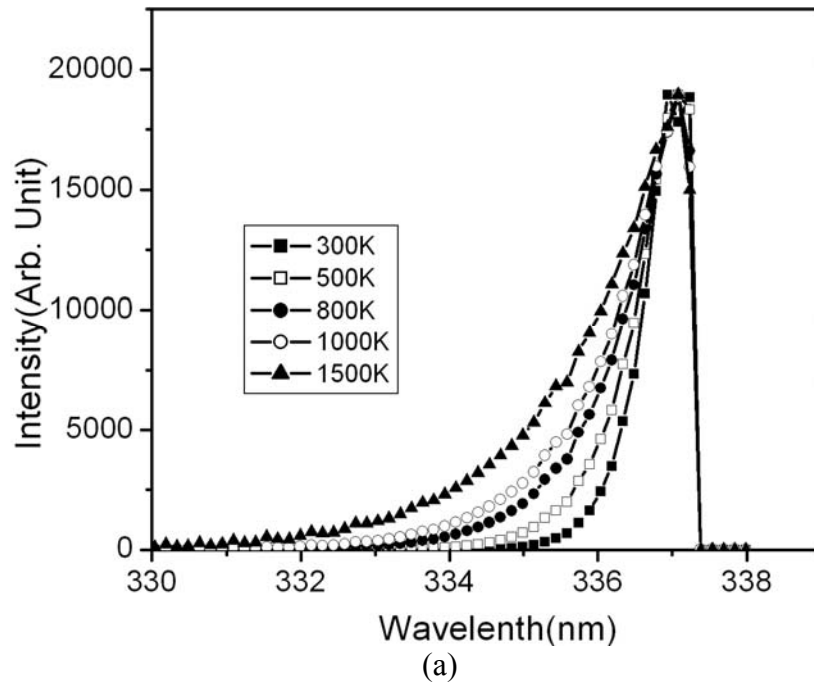
(a)

(b)

Figure 5.2   Synthetic spectrum without convolution with the instrumental function, (b) Synthetic spectrum convoluted with a Gaussian instrumental function with the resolution around 0.9nm.

Figure 5.2 (a) shows the synthetic spectrum at different rotational temperature before convolution with the instrumental function. It is observed that the spectrums form a sharp peak around 337.1 nm but are broadened as the rise of the rotational temperature and shift slightly to the shorter wavelength direction. This is reasonable since a higher temperature may correspond to a higher rotational energy level, which corresponds to a shorter wavelength. After convolution with the instrumental function, the spectrum are obviously broadened compared with those before convolution and spread to about 339.5 nm as shown in Fig. 5.2 (b).

5.3 Optical Emission Spectroscopy

The light emitted from the plasma contains important information about the various species in the plasma. An optical imaging technique is required in order to obtain and analyze local information from the radiation from the plasma. This technique is what we called optical emission spectroscopy (OES). In OES, we measure spectra emitted by atoms and ions with optical transitions in the wavelength range from about 100 nm to 900 nm. This range includes the ultraviolet, and visible light (from violet at 380 nm to red at 760 nm), and the near infrared. Using OES, we can:

(1) Determine the composition of solids, liquids, and gases.

(2) Monitor the deposition of layered devices used in the semiconductor industry, and the deposition of hard coatings on tools.

(3) Study the inner workings of atoms and ions and molecules. We can understand the behavior of the chemicals that compose the world we live in better if we know their electronic structure.

(4) The elements that make up the sun and the stars can also be determined by using

OES.

Here we will use the OES to detect the rotational structure of the emission from

N_2 $C^3\Pi_u$ to $B^3\Pi_g$ ($v'=0, v''=0$).

Usually, as the detected light originates not only from the focus point (S) of the

imaging system, but also from adjacent volumes, it is impossible to measure the local

emission signal directly. Generally, the measured emission is integrated along a line of

sight, which is determined by the small opening angle of the detection system D, or by an

aperture P as shown in Fig. 5.3.
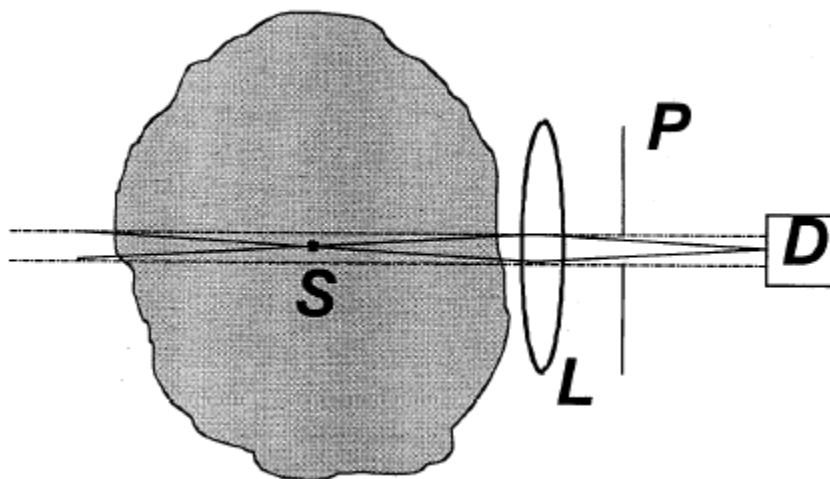
Figure 5.3   Typical arrangement of an OES system.

Optical emission spectroscopy comprises several techniques that form the most

important means we have for chemical analysis.

Spectrometer

In a spectrometer, collimated light strikes the grating and is dispersed into

individual wavelengths (colors). Each wavelength leaves the grating at a different angle

and is re-imaged by a focusing mirror onto the intensifier photocathode at the exit focal

plane. Essentially, what a spectrograph does is to form an image of the entrance slit in the exit focal plane with each position in the plane representing a different wavelength. As each wavelength images at a different horizontal position, the spectrum of the input light is detected by the detection system. In our case, the spectrum is spread over the ICCD. Individual wavelengths focused at different horizontal positions along the exit port of the spectrograph are detected simultaneously. Rotating the diffraction grating scans wavelengths across the CCD, allowing the intensity at individual wavelengths to be readily measured.

ICCD Camera

The detection system used in this experiment is a PI-MAX 1024×256 Gen. II intensified CCD (ICCD) camera with an ST133 Controller (Princeton Instruments). Usually, an ICCD camera is used for applications in general macro imaging and microscopy imaging. It is ideal for applications involving ultra low light measurements, or measurements of transient effects. In the ICCD, the detection path is as follows: A photon is incident on the intensifier photocathode and generates a photoelectron. The photoelectron is accelerated across a 200 μm gap to the front surface of the micro channel plate because of its negative charge. The electron is multiplied by successive collisions with the channel wall after entering one of the channels. When the electrons exit the micro channel, it is pulled across a 1 mm gas and strikes the phosphor screen. The kinetic energy of the electron packet is converted by the phosphor into visible photons that are then coupled through a fiber-optic bundle to the CCD. The image is read out to the Controller after being detected by the CCD and will be digitized and then transferred to the computer for processing via a high-speed link.

5.4 OES System Used in Experiment

Figure 5.4 shows the setup used in this experiment. The ICP sources and vacuum system have been characterized in Chapter 2. And only a brief description about the spectroscopy equipment will be given here.
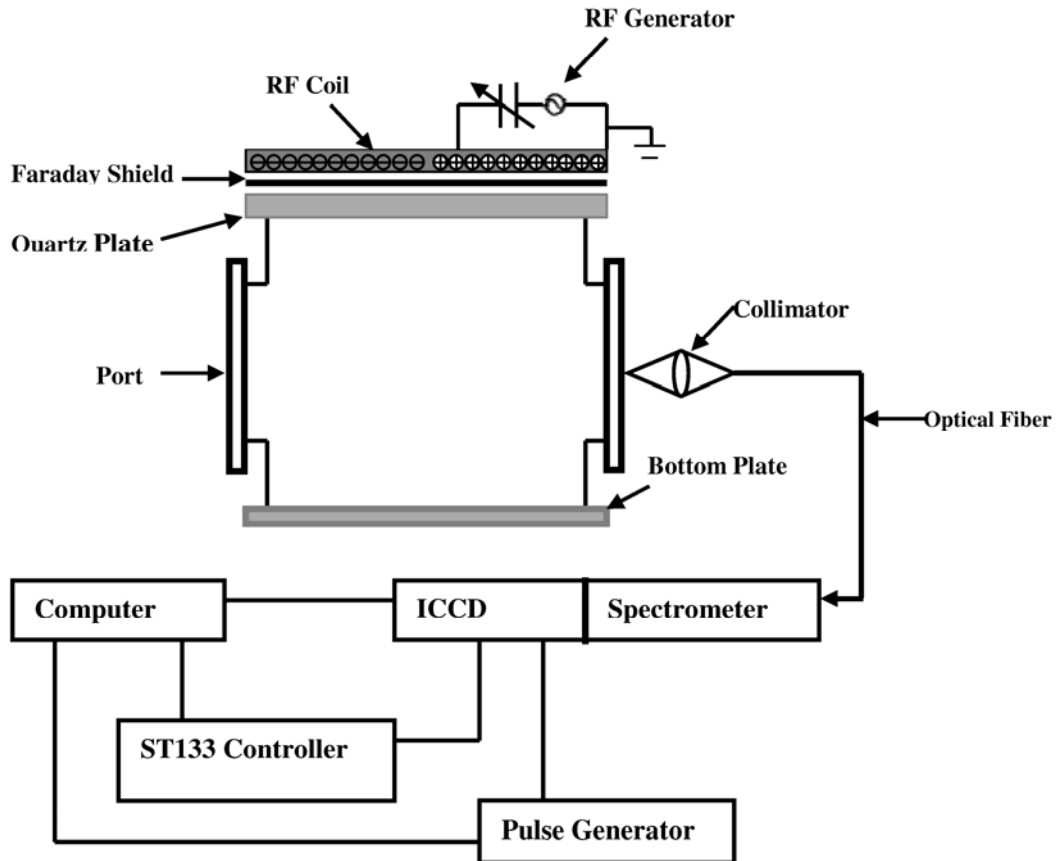
Figure 5.4   Experimental Set-up.

The optical emission spectrometer (OES) system consists of a SpectraPro 300i imaging spectrometer with a 0.3 m focal length (Acton Research Corporation), a PI-MAX 1024×256 Gen. II intensified CCD (ICCD) camera with an ST133 Controller (Princeton Instruments), a DG535 Timing Generator (Stanford Research Systems, Inc.), and a computer with Winspec data acquisition software. A home-made collimator, made

of a plano-convex quartz lens of a focal length of 5 cm and diameter of 1.3 cm, collects the nearly parallel light entering the collimator and focuses the light onto one end of a quartz optical fiber which guides the light to the entrance port of the spectrometer. The fiber diameter of 25 μm defines the entrance slit width. A 600 grooves/mm BLZ=300 nm grating (the blazed gratings are optimized at 300 nm) has been used to disperse the incoming plasma emission. The ICCD camera records dispersed spectrum at the focal plane of the exit slit. The pixel size of the photocathode array in the ICCD camera is 25 μm. In the experiments reported in this section, the ICCD camera was usually gated for 10 seconds and 30 images was accumulated for each spectrum. Finally, the image was readout to the controller, where it was digitized and transferred via a high-speed data link to the computer for further off-line processing.

The nitrogen second positive system ($C^3\prod_u$, V'=0- $B^3\prod_g$, V''=0) was used for neutral gas temperature measurement in nitrogen and argon discharges at different gas pressures and discharge powers. For Ar discharge, 5% nitrogen of the total gas flow rate was added to the discharge gas. It is assumed that the small amount of the nitrogen will not affect Ar discharge and the Ar and N_2 temperatures are equal.

5.5 Experimental Results and Discussion

5.5.1 Typical Experimental Result

Figure 5.5 shows a typical experimental spectra and the Gaussian fitting. The image was sampled from nitrogen discharge, which was operated at 400 W, 10 mTorr. The fitted temperature is 895 K. Figure 5.6 shows the chi-square values at different fitting temperatures. The minimum χ^2 corresponds to the temperature of 895 K which is taken as the measured neutral temperature.
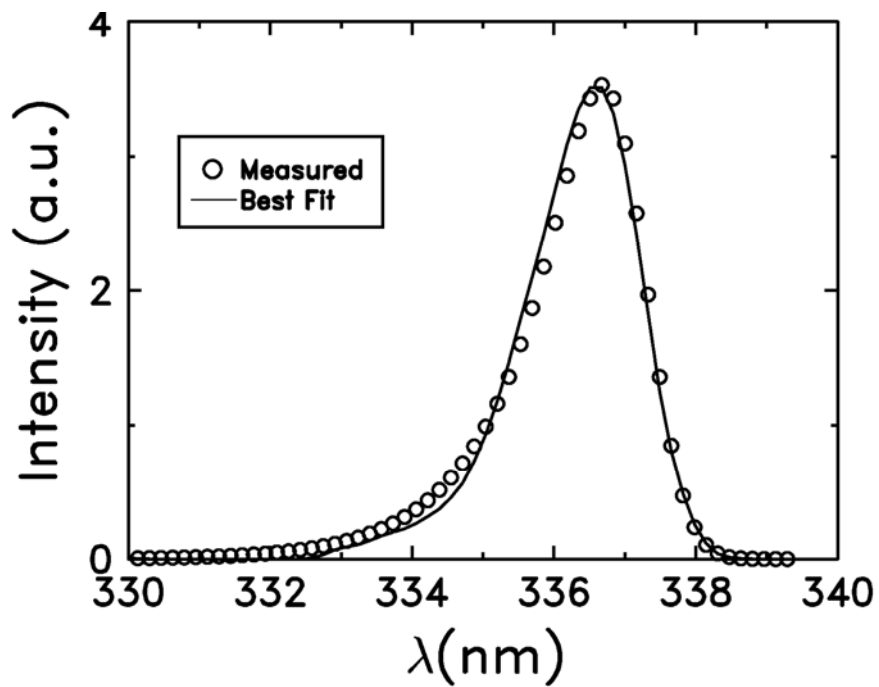
Figure 5.5   A typical experimental spectra and the corresponding fitting
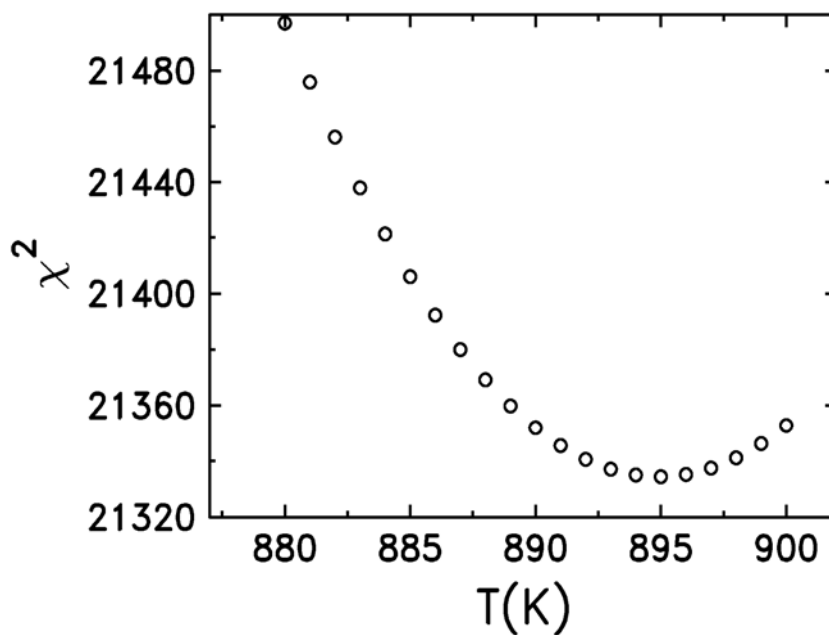

Figure 5.6   Chi-square at different temperature when fit the spectra sampled from 10 mTorr, 400 W nitrogen discharge.

The experimental results for nitrogen and argon discharges are presented in the following two subsections.

5.5.2 Argon Plasma

Dependence of the neutral temperature on the rf power is shown in Fig. 5.7 (5% nitrogen was added for diagnostics purpose). At a fixed gas pressure, the temperature does not change significantly when the discharge power increases from 100 to 600 W. This observation is different from the results reported by some other researchers [25, 26], who show an obvious increase of the neutral gas temperature with the discharge power. It is evident that the temperature can be grouped into three bands corresponding to the pressure ranges: 2-10 mTorr, 50-300 mTorr, and 500 mTorr - 1 Torr. The first temperature increase corresponds to a significant increase in the plasma density when the pressure changes from 10 mTorr to 50 mTorr as indicated by the Langmuir Probe measurement, while the reason for the second temperature increase remains unclear since the plasma density in our system peaks at around 300-400 mTorr. Table 5.1 shows the electron density in cm^{-3} at these turning points. The electron density was inferred from the electron saturation currents collected by the Langmuir probe

	100W	200W	300W	400W	500W	600W
10mTorr	4.8×10^{10}	9.3×10^{10}	1.2×10^{11}	1.5×10^{11}	2.1×10^{11}	2.8×10^{11}
50mTorr	1.3×10^{11}	3.6×10^{11}	4.5×10^{11}	6.5×10^{11}	8.0×10^{11}	1.0×10^{12}
300mTorr	2.3×10^{11}	5.3×10^{11}	9.4×10^{11}	1.0×10^{12}	1.3×10^{12}	1.7×10^{12}
500mTorr	1.6×10^{11}	4.5×10^{11}	6.4×10^{11}	8.2×10^{11}	1.1×10^{12}	1.3×10^{12}

Table 5.1   Electron density (cm^{-3}) measured with the Langmuir probe.

Figure 5.8 shows the dependence of the neutral temperature on the gas pressure. The temperature increases from approximately 840 K at 2 mTorr to 1850 K at 1 Torr.

When related to the gas pressure, the temperature is almost proportional to the logarithm of the gas pressure. This result is similar to that found by Tonnis and Graves [27] in an inductively coupled plasma abatement device and by Bai and Sawin [71] in transformer coupled toroidal argon plasmas.
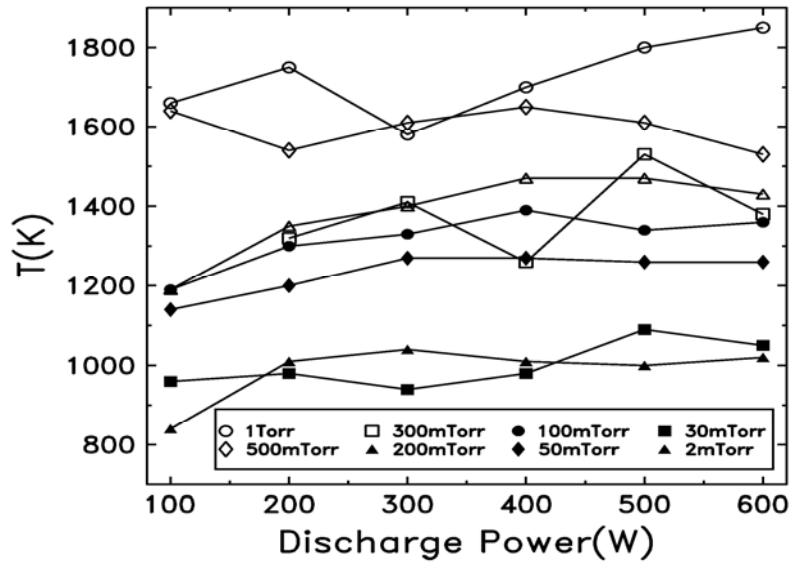

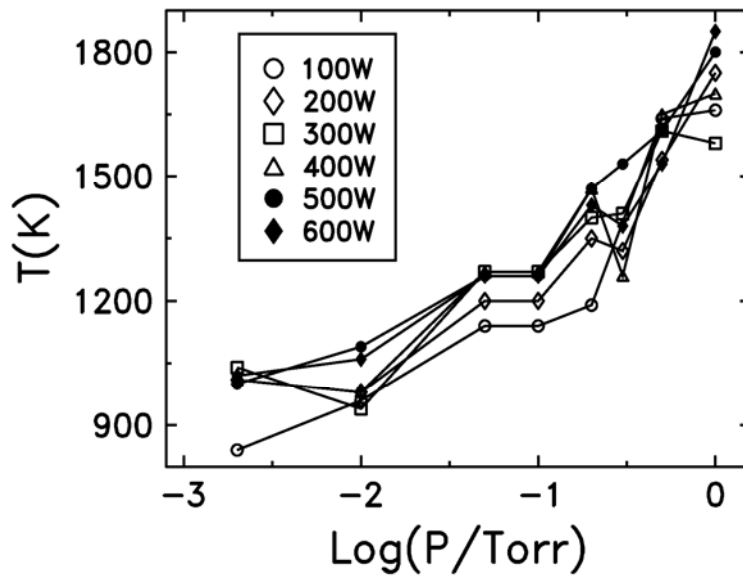Figure 5.7   Gas temperature-gas pressure in argon plasma.

Figure 5.8   Gas temperature-log(Pressure/Torr) in argon plasma.

5.5.3 Nitrogen Plasma

Figure 5.9 depicts the neutral gas temperature of the nitrogen plasmas as a function of the logarithm of the pressure. The temperature changes from 650 K at 5 mTorr, 100 W to almost 1300 K at 200 mTorr, 600 W. For a given discharge power, when the pressure is low, the temperature is approximately linear with the logarithm of the pressure. However, when the pressure further increases, the temperature drops sharply, especially at a low discharge power. This transition pressure increases with the discharge power (20 mTorr for 100 W, 50 mTorr for 200 W, and 50 mTor for 300 W). At higher powers (400 W, 500 W, and 600 W), the transition points did not occur up to 200 mTorr. It is expected that the transition should occur at even higher pressure. However, in our ICP device, it is difficult to have stable discharge when the nitrogen gas pressure is higher than 200 mTorr. Combined with other observations, such as plasma density and optical emission, the reduction in the neutral temperature also corresponds to a transition from the H-mode to E-mode. Furthermore, at higher pressures, higher discharge power is needed to sustain the H-mode.
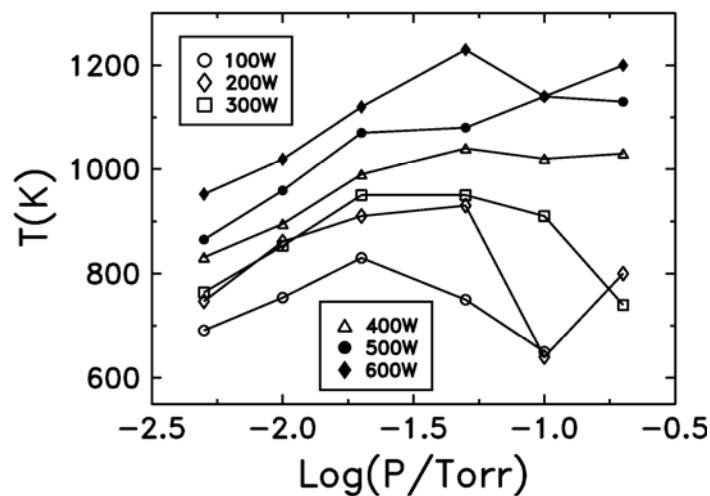

Figure 5.9   Gas temperature-log(Pressure/Torr) at different discharge powers in nitrogen plasma.

Figure 5.10 shows the dependence of the gas temperature on the discharge power. In contrast to the insensitivity of the neutral gas temperature to the discharge power in the argon plasma, the neutral temperature in the nitrogen plasma increases linearly with the discharge power in the H-mode discharge corresponding to all the data points for the low pressure (5 mTorr – 20 mTorr) discharges. The deviation of the temperature data points from a straight line for higher pressures (50 mTorr, 100 mTorr, and 200 mTorr) and lower powers corresponds to the E-mode discharges. Figure 5.10 again shows that at a fixed higher pressure, there is a threshold discharge power to realize transition from E-mode to H-mode.
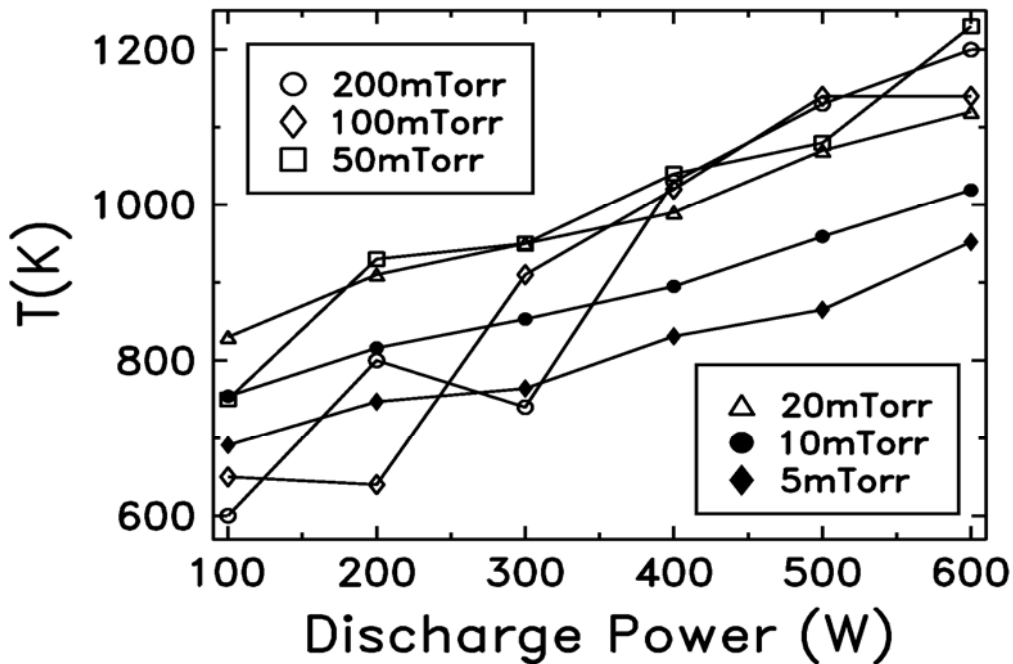

Figure 5.10   Gas temperature-discharge power at different working pressures in nitrogen plasma.

It is believed that discharges in molecular gases contain several neutral heating mechanisms which are not present in discharges in atomic gases, such as Franck-Condon

heating, thermalization of electron impact vibrational excitation products that releases vibrationally and/or electronically excited metastable species back to the bulk discharge. And the nitrogen discharge may exhibit higher neutral temperatures even at lower plasma densities [26]. By comparing the experimental results in the argon and nitrogen discharges, however, it is found that for the same discharge conditions, the neutral temperature in the argon plasma is usually higher than that in the nitrogen plasma in contrast to the result reported in ref. [26]. The discrepancy may be attributed to the lower plasma density in the nitrogen discharge which has been verified by the data from Langmuir Probe measurements. It is not surprising to find a lower neutral temperature in low-density plasma since the major mechanism of heating neutrals is the electron neutral collisions. The heat transfer to the neutral species through e-n collisions is proportional to the plasma density and neutral gas density: $W_{heat} \propto n_e n_n <\sigma v>$. As a result, the heating effect caused by the much lower density of the nitrogen plasma as compared with the argon plasma might outweigh the effect caused by those mechanisms unique in the molecular gases.

Chapter 6

Conclusions and Suggestions for Future Research

The single Langmuir probe and optical emission spectroscopy have been used to analyze the inductively coupled plasma of atomic gases (argon and helium) and molecular gases (nitrogen and hydrogen) over a wide range of gas pressures and rf powers.

Information about the EEDF has been obtained by using the ac method via the radially tunable probe. The results in atomic gases show a change to Druyvesteyn-like distribution in EEDF due to the heating mechanism transition to collisional heating as a result of the increasing gas pressure. In 1 mTorr argon plasma, the EEDF shows a two temperature structure and this might be caused by the rapid diffusion of the high-energy electrons to the chamber wall. The EEDF in argon plasma shows non-local property at the pressure of 1 mTorr and this can be verified by the small variation of the average electron energy. The non-locality still holds at 10 mTorr although the variation in $\langle \varepsilon \rangle$ increases slightly. The variation reaches up to 14.5% when the pressure increases to 50 mTorr. The significant variation of the $\langle \varepsilon \rangle$ indicates that the applicability of non-local theory becomes invalid at this high pressure.

EEDF in molecular gases nitrogen and hydrogen is distinct from what has been reported and is always accompanied by an extra peak. This might be caused by the super-

68

elastic collisions which transfer energy from the vibrational or electronic excited states to the electrons. This phenomenon is more obvious at a low local electric field, under which condition the vibrational and electronic excited states of molecules are populated.

The average electron energy in argon plasma shows a decreasing when the gas pressure is increased as a result of the inelastic collisions which transfer energy from the high energy electrons to the neutrals and this is consistent with the power balance equation. Regarding the rf power, the increase of the average electron energy at low pressures might be caused by the heating of neutrals, which leads to a decrease of the neutral number density, and thus an increase of the average electron energy. When compared with the average electron energy of helium gas, it is found that the $\langle \varepsilon \rangle$ of argon is lower than that of helium. This is normal since the ionization threshold energy of helium is higher than that of argon.

Plasma density in argon discharge is in the range of $10^{10} - 10^{12} / \text{cm}^3$ and peaks around 300 mTorr. Any further increase of the neutral gas pressure leads to a decrease of the plasma density. The result can be explained by the power balance relation.

Significant heating of neutrals in the ICP has been verified by the optical emission spectroscopy measurement. The temperatures measured are several times higher than the room temperature with the maximum one reaches as high as 1800 K in argon plasma. The electron density plays an important role in controlling the neutral gas temperature. In the H-mode argon and nitrogen discharges with high densities, the neutral temperature is almost proportional to the logarithm of the gas pressure. The effect of the rf power on the neutral gas temperature is more significant in the nitrogen plasma. The neutral gas temperature increases almost linearly with the rf power in nitrogen plasma while it

remains almost constant in the argon plasma. Due to the much lower plasma density in nitrogen, the neutral temperature is found to be lower than that of argon under the same discharge condition. The discharge mode transition can also be observed from the jumps of the neutral gas temperature from a high temperature to a lower one when increases the gas pressure at a fixed discharge power. The discharge mode transition has also been verified by the plasma density.

Below are some suggestions for future work regarding this study:

(1) Improve the probe circuit to minimize the circuit resistance and check whether the transition to Druyvesteyn distribution with the increasing rf power is caused by the large circuit resistance.

(2) Measurements of vibrational and electronic excited states in molecular gases might be helpful to find out how they affect the formation of EEPF exactly.

(3) Local electric field measurement is necessary in order to evaluate the effect of super-elastic collisions.

(4) Extending this work to the processing plasmas.

LIST OF REFERENCES

[1]   Chen F F 1984 *Introduction to Plasma Physics and Controlled Fusion* (Plenum Press, New York).

[2]   Rossnagel S M, Cuomo R J and Westwood W D 1990 *Handbook of Plasma Processing Technology* (Noyes Publications, Park Ridge, N.J.).

[3]   Lieberman M A and Lichtenberg A J 1994 *Principles of Plasma Discharges and Materials Processing* (Wiley, New York).

[4]   Brisol R J 1995 *Industrial Plasma Engineering* **2** (Institute of Physics Pub, Philadelphia) .

[5]   Grill A 1994 *Old Plasma in Materials Fabrication. From Fundamental to Applications* (IEEE, New York).

[6]   Popov O 1995 *High Density Plasma Sources* (Noyes, Park Ridge, NJ).

[7]   Conrads H and Schmidt M 2000 *Plasma Sources Sci. Technol.* **9** 441.

[8]   Toader E I 2004 *Plasma Sources Sci. Technol.* **13** 646.

[9]   Bibinov N K, Kokh D B, Kolokolov N B, Kostenko V A, Meyer D, Vinogradov I P and Wiesemann K 1998 *Plasma Sources Sci. Technol*. **7** 298.

[10] Godyak V A, Piejak R B and Alexandrovich B M 1995 *Plasma Sources Sci. Technol.* **4** 332.

[11] Ramamurthi B, Economou D J and Kaganovich I D 2003 *Plasma Sources Sci. Technol.* **12** 302.

[12] Ramamurthi B, Economou D J and Kaganovich I D 2003 *Plasma Sources Sci. Technol.* **12** 170.

[13] Gudmundsson J T, Kimura T and Lieberman M A 1999 *Plasma Sources Sci. Technol.* **8** 22.

[14] Barnes M S, Forster J C, and Keller J H 1993 *App. Phys. Lett*. **62** 21.

[15] Seo S H, Kim S S, Hong J I, Chang C S, and Chang H Y 2000 *Appl. Phys. Lett*. **76** 149.

[16]   Kim S S, Chung C W, Chang H Y 2003 *The Solid Thin Films* **435** 72

[17] Godyak V A, Piejak R B and Alexandrovich B M 2003 *Plasma Sources Sci. Technol.* **11** 525.

71

[18] Godyak V A and Kolobov V I 1998 *Phys. Rev. Lett.* **81** 369.

[19] Godyak V A, Piejak R B and Alexandrovich B M 1992 *Plasma Sources Sci. Technol.* **1** 36.

[20] Godyak V A, Piejak R B and Alexandrovich B M 1993 *J. Appl. Phys.* **73** 3657.

[21] Mahoney L J, Wendt A E, Barrios E, Richards C J and Shohet L J 1994 *J. Appl. Phys.* **76** 2041.

[22] Kortshagen U, Pukropski I, and zethoff M 1994 *J. Appl. Phys.* **76** 2048.

[23] Singh H and Graves D B 2000 *J. Appl. Phys.* **87** 4098.

[24] Singh H and Graves D B 2000 *J. Appl. Phys.* **88** 3389.

[25] Donnelly V M and Malyshev M V 2000 *Appl. Phys. Lett.* **77** 2467.

[26] Tonnis E J and Graves D B 2002 *J. Vac. Sci. Technol. A* **20** 1787.

[27] Ostrikov K N, Denysenko I B, Tsakadze E L, Xu S and Storer R G 2002 *J. App. Phys.* **92** 4935.

[28] Hash D B, Bose D, Rao M V V S, Cruden B A, Meyyappan M and Shama S P 2001 *J. Appl. Phys.* **90** 2148.

[29] Hebner G A 1996 *J. Appl. Phys.* **80** 2624.

[30] Hebner G A and Miller P A 2000 *J. Appl. Phys.* **87** 8304.

[31] Hebner G A 2001 *J. of Appl. Phys.* **89** 900.

[32] Sing H, Coburn J W and Graves D B 2001 *J. Vac. Sci. Techonol. A* 19 718.

[33] Abada H, Chabert P, Booth J P and Robiche J 2002 *J. Appl. Phys.* **92** 4223.

[34] Bol'shakov A A, Cruden B A and Sharma S P 2004 *Plasma Sources Sci. Technol.* **13** 691.

[35] Malyshev M V, Donnely V M, Downey S W, Colonell J I and Layadi N 2000 *J. Vac. Sci. Technol. A* **18** 849.

[36] Kiehlbauch M W and Graves D B 2001 *J. Appl. Phys.* **89** 2047.

[37] Ostrikov K N, Denysenko I B, Tsakadze E L, Xu S and Storer R G 2002 *J. App. Phys.* **92** 4935.

[38] Hash D B, Bose D, Rao M V V S, Cruden B A, Meyyappan M and Shama S P 2001 *J. Appl. Phys.* **90** 2148.

[39] Schoenberg K F, 1980 *Rev. Sci. Instr.* **51** 1159.

[40] Oh B H, Choi B H, Xiao C and Hirose A 1998 *Journal of Accelerator and Plasma Research* **3** 77.

[41] Moore G L 1989 *Introduction to Inductively Coupled Plasma Atomic Emission Spectrometry* **3** (Elsevier, New York).

[42] Reed T B 1961 *J. Appl. Phys.* **32** 821.

[43] Zeuner M and Neumann H 1997 *J. Appl. Phys.* **81** 2985.

[44] Huddlestone R H and Leonard S L 1965 *Plasma Diagnostic Techniques* (Academic Press, Los Anageles).

[45] Auciello O and Flamm D L 1989 *Plasma Diagnostics* **1** (Academic Press, Boston).

[46] Swift J D and Schar M J R 1970 *Electrical Probes for Plasma Diagnostics* (lliffe, London).

[47] Hopwood J, Guarnieri C R, Whitechair S J and Cuomo J J 1993 *J. Vac. Sci. Technol. A* **11** 147.

[48] Hori T, Bowden M D, Uchino K and Muraoka K 1996 *Appl. Phys. Lett.* **69** 24.

[49] Pu Y K, Guo Z G, Rehman A U, Yu Z D, Ma J 2006 *Plasma Phys. Control. Fusion* **48** 61.

[50] Karoulina E V and Lebedev Y A 1988 *J. Phys. D* **21** 411.

[51] Trunec D, Spanel P, Smith D 2003 *Chem. Phys. Lett.* **372** 728.

[52] Kolobov V I and Hitchon W N G 1995 *Phys. Rev. E* **52** 972.

[53] Mumken G 1999 *J. Phys. D: Appl. Phys.* **32** 804.

[54] Capitelli M, Colonna G, Gicquel A, Gorse C, Hassouni K and Longo S 1996 *Phys. Rev. E* **54** 1843.

[55] Colonna G, Gorse C, Capitelli M, Winkler R, and Wilhelm J 1993 *Chem. Phys. Lett.* **5** 213.

[56] Capitelli M, Gorse C and Longo S 1998 *J. Thermophysics and Heat Transfers* **12** 478.

[57] Tan W P S 1973 *J. Phys. D: Appl. Phys.* **6** 1206.

[58] Malyshev M V and Donnelly V M 1999 *J. Appl. Phys*. **87** 1642.

[59] Schwabedissen A, Benck E C and Roberts J R 1997 *Physical Review E* **55** 3450.

[60] Jang S S and Lee W J 2001 *J. Vac. Sci. Technol. A* **19** 2335.

[61] Cruden B A, Rao M V V S, Sharma S P, and Meyyappan M 2002 *Appl. Phys. Lett.* **81** 990.

[62] Cruden B A, Rao M V V S, Sharma S P and Meyyappan M 2002 *J. Appl. Phys.* **91** 8955.

[63] Schabel M J, Donnelly V M, Kornlit A and Tai W W 2002 *J. Vac. Sci. Technol. A* **20** 555.

[64] Palmero A, Cotrino J, Barranco A and Gonzalez-Elipe A R 2002 *Phys. of Plasmas* **9** 358.

[65] Davis G P and Gottscho R A 1983 *J. Appl. Phys.* **54** 3080.

[66] Linss V 2005 *Spectrochimica Acta Part B* **60** 253.

[67] Herzberg G 1939 *Molecular Spectra and Molecular Structure. IV. Constants of Diatomic Molecules* (Prentice-Hall, New York).

[68] Chelouah A, Marode E, Hartmann G and Achat S 1994 *J. Phys. D: Appl. Phys.* **27** 940.

[69] Shali K, Hochard L and Pointu A M 1993 *Meas. Sci. Technol.* **4** 685.

[70] Gardet G, Moulard G, Courbon M, Rogemond M and Druetta M 2000 *Meas. Sci. Technol.* **11** 333.

[71] Bai B and Sawin H 2004 *J. Vac. Sci. Technol. A* **22** 2014